Cell Reports

Article

Oligomerized liprin-α promotes phase separation of ELKS for compartmentalization of presynaptic active zone proteins

Graphical abstract

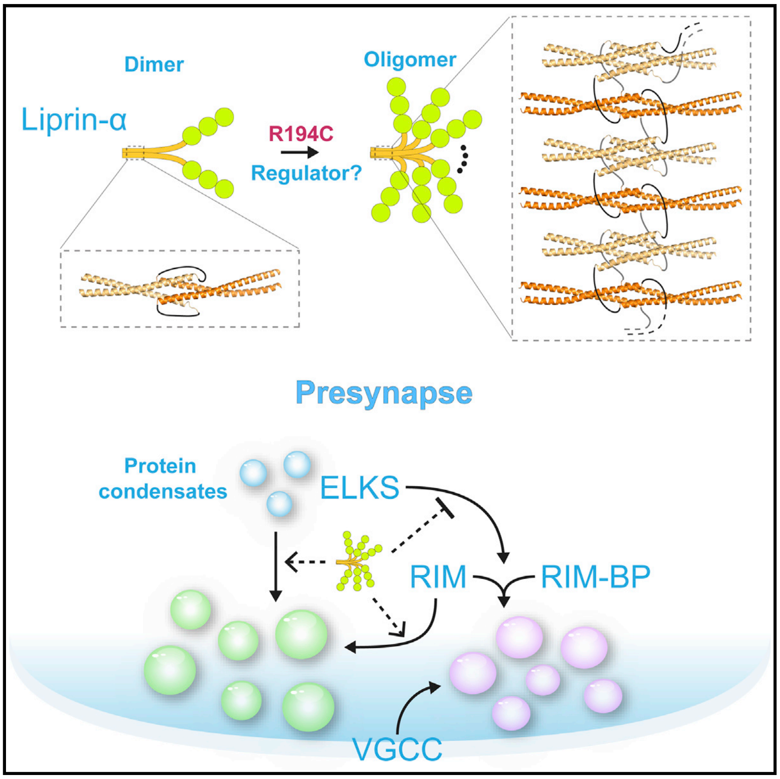

Highlights

- Liprin-α2 is self-assembled via the N-terminal conserved coiled coil
- The R194C mutation promotes liprin-α2 oligomerization
- Oligomerized liprin-α2 coiled coils alter the phase separation of ELKS
- Liprin-α2 determines the active zone protein distribution in protein condensates

Authors

Mingfu Liang, Gaowei Jin, Xingqiao Xie, ..., Fengfeng Niu, Cong Yu, Zhiyi Wei

Correspondence

yuc@sustech.edu.cn (C.Y.),
weizy@sustech.edu.cn (Z.W.)

In brief

Presynaptic active zone formation requires scaffold proteins, including liprin-α and ELKS. Liang et al. report the self-assembly mechanism of liprin-α2 and its role in regulating the condensate formation of ELKS and other active zone proteins, which sheds light on the active zone assembly.

Liang et al., 2021, Cell Reports *34*, 108901
March 23, 2021 © 2021 The Author(s).
https://doi.org/10.1016/j.celrep.2021.108901

CellPress

Cell Reports

CellPress
OPEN ACCESS

Article

Oligomerized liprin-α promotes phase separation of ELKS for compartmentalization of presynaptic active zone proteins

Mingfu Liang,[1,5] Gaowei Jin,[1,5] Xingqiao Xie,[1,2,5] Wenchao Zhang,[1] Kaiyue Li,[1] Fengfeng Niu,[1,2] Cong Yu,[1,3,*] and Zhiyi Wei[1,2,4,6,*]
[1]Department of Biology, Southern University of Science and Technology, Shenzhen, Guangdong 518055, China
[2]Academy for Advanced Interdisciplinary Studies, Southern University of Science and Technology, Shenzhen, Guangdong 518055, China
[3]Guangdong Provincial Key Laboratory of Cell Microenvironment and Disease Research, and Shenzhen Key Laboratory of Cell Microenvironment, Shenzhen, Guangdong 518055, China
[4]Brain Research Center, Southern University of Science and Technology, Shenzhen, Guangdong 518055, China
[5]These authors contributed equally
[6]Lead contact
*Correspondence: yuc@sustech.edu.cn (C.Y.), weizy@sustech.edu.cn (Z.W.)
https://doi.org/10.1016/j.celrep.2021.108901

SUMMARY

Synaptic scaffold proteins (e.g., liprin-α, ELKS, RIM, and RIM-BP) orchestrate ion channels, receptors, and enzymes at presynaptic terminals to form active zones for neurotransmitter release. The underlying mechanism of the active zone assembly remains elusive. Here, we report that liprin-α proteins have the potential to oligomerize through the N-terminal coiled-coil region. Our structural and biochemical characterizations reveal that a gain-of-function mutation promotes the self-assembly of the coiled coils in liprin-α2 by disrupting intramolecular interactions and promoting intermolecular interactions. By enabling multivalent interactions with ELKS proteins, the oligomerized coiled-coil region of liprin-α2 enhances the phase separation of the ELKS N-terminal segment. We further show that liprin-α2, by regulating the interplay between two phase separations of ELKS and RIM/RIM-BP, controls the protein distributions. These results imply that the complicated protein-protein interactions allow liprin-α to function with the active zone scaffolds and compartmentalize protein assemblies to achieve comprehensive functions in the active zone.

INTRODUCTION

Neuronal signals are transmitted from a neuron to its target cell through specialized cell-cell junctions termed synapses. Synaptic transmission relies on the appropriate docking, priming, and fusion of synaptic vesicles at presynaptic terminals during neurotransmitter release in response to channel-dependent Ca^{2+} influx triggered by action potentials (Südhof, 2013). These processes are spatiotemporally controlled through a protein-dense apparatus attached to the presynaptic plasma membrane, called the "active zone" (Sigrist and Schmitz, 2011; Südhof, 2012). Presynaptic active zones are precisely aligned with the postsynaptic densities and allow the released neurotransmitters to be efficiently perceived by receptors anchored at the postsynaptic densities. Extensive research on the active zone has revealed several core components, including liprin-α, glutamine/leucine/lysine/serine-rich protein (ELKS), Rab3a-interacting molecule (RIM), RIM-binding protein (RIM-BP), Bassoon/Piccolo, and Munc13 (Biederer et al., 2017; Emperador-Melero and Kaeser, 2020; Petzoldt et al., 2016; Südhof, 2012). Studies using electron tomography and super-resolution light microscopy have shown that these active zone scaffolds are unevenly distributed in specific patterns within the active zone to create nanoscale release sites for synaptic vesicles (Biederer et al., 2017; Böhme et al., 2016; Sakamoto et al., 2018; Tang et al., 2016). The mechanism by which the active zone proteins are coordinated for the dynamic assembly in an organized manner remains largely unknown. Recently, RIM and RIM-BP were found to form a condensate via liquid-liquid phase separation (LLPS) and consequently promote Ca^{2+} channel clustering (Wu et al., 2019), suggesting an assembly model for the active zone. However, depletion of RIM or RIM-BP affects the active zone ultrastructure only mildly, while the combinatorial deletion of RIM/RIM-BP or RIM/ELKS can profoundly disrupt the structure and function of the active zone (Acuna et al., 2016; Wang et al., 2016). Hence, the interconnected scaffolds function together and provide redundancy in mediating the assembly of the active zone through an unknown mechanism.

Among these active zone scaffolds, liprin-α plays critical roles in organizing the protein assemblies of the active zone. In *C. elegans* and *Drosophila*, the dysfunction of the liprin-α homologs (SYD2 and Dliprin-α, respectively) leads to altered active zone morphology and reduced synaptic vesicle accumulation (Kaufmann et al., 2002; Zhen and Jin, 1999). A further electron

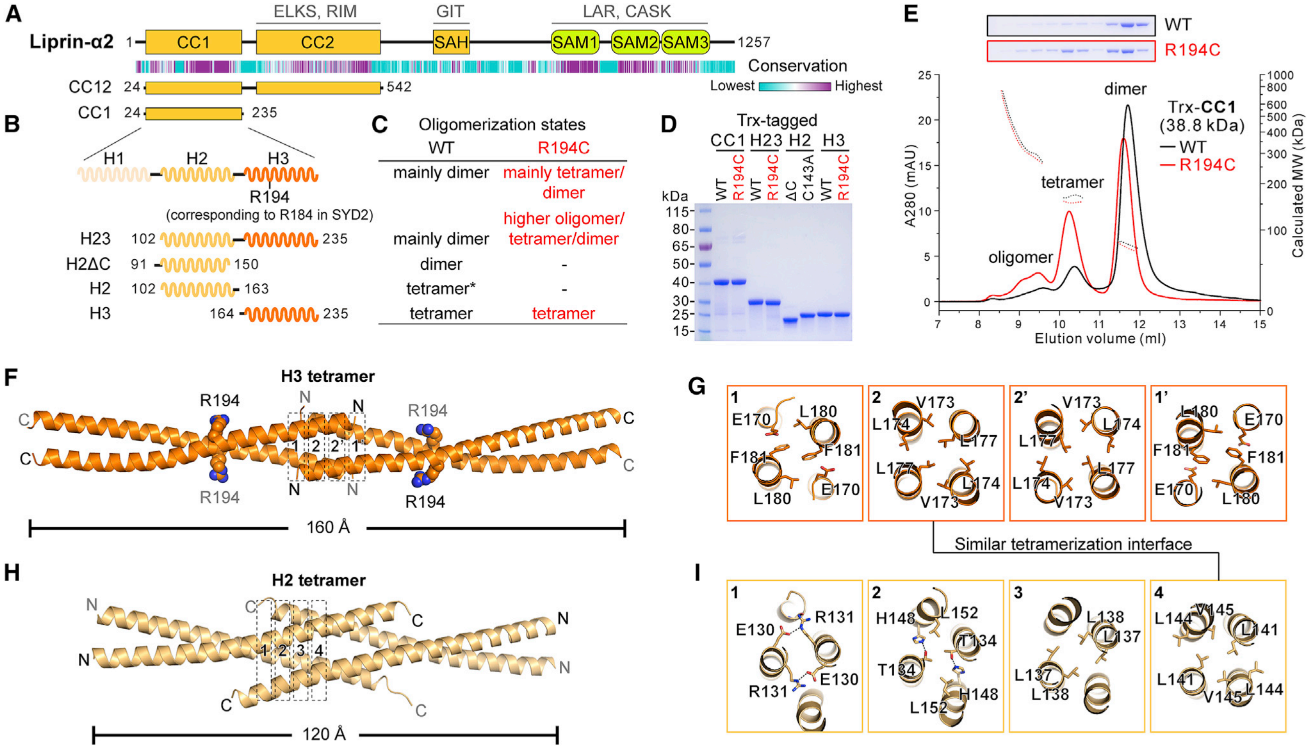

Figure 1. Biochemical and structural analysis of coiled-coil-mediated oligomerization in the highly conserved CC1 region of liprin-α2

(A) Schematic diagrams showing the domain organizations of liprin-α2. The heatmap below shows the amino acid sequence conservation of liprin-α proteins. The presynaptic proteins that interact with liprin-α are indicated above their corresponding binding regions.

(B) Three coiled-coil helices in the CC1 region and their abbreviations (H1, H2, and H3) used in this study. The position of the gain-of-function-mutation was indicated.

(C) Summaries of oligomeric states of different CC1 boundaries as shown in (B). The H2 fragment used for analysis containing the C143A mutation is also shown.

(D) SDS-PAGE analysis showing the purities of the CC1 boundaries used for measuring oligomeric states as shown in (C).

(E) Analytical gel filtration analysis showing the oligomeric states of CC1-WT and R194C. The indicated molecular weight was measured by a following MALS analysis. The theoretical molecular weight of Trx-tagged CC1 was indicated. The fractions were harvested and shown in SDS-PAGE.

(F) Overall structure of the H3 tetramer. Two H3 coiled-coil dimers interact with each other via their N termini to form a tetramer. The sidechains of R194 in the tetramer are highlighted.

(G) Molecular details of the tetramerization interface for the H3 tetramer.

(H) Overall structure of the H2 tetramer. Two H2 coiled-coil dimers interact with each other via their C termini to form a tetramer.

(I) Molecular details of the tetramerization interface for the H2 tetramer. Hydrogen bonds and salt bridges are indicated by dashed lines.

See also Figures S1 and S2.

microscopic (EM) investigation showed that SYD2 determines the size of electron-dense projections, the characteristic structure in the active zone (Kittelmann et al., 2013). The mammalian liprin-α family consists of four members, liprin-α1/2/3/4, among which liprin-α2 and liprin-α3 are highly expressed in the brain (Spangler et al., 2011; Zürner and Schoch, 2009; Zürner et al., 2011). Depletion of liprin-α2 or liprin-α3 in mice results in the disruption of synaptic transmission and active zone ultrastructure (Spangler et al., 2013; Wong et al., 2018). As an early organizer in the active zone assembly, liprin-α recruits a variety of proteins that are involved in neurotransmitter release (e.g., ELKS, RIM, G-protein-coupled receptor-kinase-interacting protein (GIT), leukocyte common antigen-related receptor (LAR) and calcium/calmodulin-dependent serine protein kinase (CASK)) (Ackley et al., 2005; Kaufmann et al., 2002; Olsen et al., 2005; Patel et al., 2006; Spangler et al., 2013; Wong et al., 2018), mediated by the N-terminal coiled coils, the middle single-α-helical (SAH) region, and the C-terminal sterile-alpha-motif (SAM) domains of liprin-α, respectively (Ko et al., 2003; Liang et al., 2019; Serra-Pagès et al., 1998; Wei et al., 2011) (Figure 1A). Genetic studies identified a missense mutation (R184C) in SYD2 that can bypass the genetically introduced defects of active zone formation and enlarge the dense projections in an ELKS-dependent manner (Dai et al., 2006; Kittelmann et al., 2013). This gain-of-function mutation is located at a coiled-coil region (CC1) that is mostly conserved in the liprin-α proteins across different species (Figures 1A and S1). Although the R184C mutation was proposed to drive the self-association of synapse defective 2 (SYD2) protein and enhance the binding of SYD2 to ELKS (Dai et al., 2006; Kittelmann et al., 2013), the underlying mechanism of the gain-of-function effect induced by R184C remains unclear due to very limited biochemical and structural characterizations.

Here, we revealed that the strictly conserved arginine residue, corresponding to R194 in human liprin-α2, stabilizes the intramolecular interaction in the CC1 region. The disruption of the intramolecular interaction results in the oligomerization of either CC1 or the entire coiled-coil region of liprin-α2. Interestingly, the highly oligomerized liprin-α2_CC12 interacts with ELKS and promotes the LLPS of ELKS by promoting multivalent interactions. The involvement of liprin-α2 in the LLPS of ELKS modifies the protein assembly in the condensed phase, preventing ELKS from entering the RIM/RIM-BP condensate and increasing the capability of ELKS in recruiting the RIM proteins into the ELKS condensate. In contrast to the RIM/RIM-BP condensate, the highly concentrated RIM proteins in the ELKS condensate fail to enrich Ca^{2+} channel proteins. Our findings provide a potential explanation not only for the gain-of-function effect of the liprin-α/SYD2 mutant in active zone assembly, but also for the role of liprin-α in controlling the compartmentalization and function of active zone proteins.

RESULTS

The R194C mutation enhances the oligomerization of liprin-α2_CC1

A sequence analysis indicated that the highly conserved CC1 region of liprin-α contains three α-helical coiled coils, hereafter referred to as H1, H2, and H3 (Figures 1B and S1). To dissect the potential effect of the substitution of R194 with a cysteine on these proteins, we purified the CC1 fragment of liprin-α2 (liprin-α2_CC1) with or without the R194C mutation and measured the molecular mass by using multiangle light scattering (MALS) (Figures 1B–1D). In line with a previous observation suggesting that SYD2_CC1 forms a homodimer (Taru and Jin, 2011), the wild-type (WT) liprin-α2_CC1 protein was predominantly dimerized (Figure 1E). However, the R194C mutant of liprin-α2_CC1 had a much greater tendency to form a tetramer or higher-level oligomers (Figure 1E; to simplify description, ‘‘oligomer’’ was used hereafter to indicate an oligomer having more than four repeating molecules). Likewise, the fragment containing H2 and H3 (H23) showed similar dimer formation in analytical gel filtration analysis, while the R194C mutation promoted oligomer formation of H23 (Figure S2A). Adding 10 mM DTT in protein buffer had little effect on the R194C-promoted oligomerization of liprin-α2_CC1 (Figure S2B), suggesting that the oligomerization of the CC1 fragment is unlikely due to disulfide cross-linking through the mutation-introduced cysteine. Since R194 is strictly conserved in liprin-α family members (Figure S1), we speculate that R194 prevents the CC1 region from forming tetramers/oligomers by stabilizing the CC1 dimer.

To determine the role of R194 in maintaining the CC1 dimer, we first analyzed the molecular mass of the H3 fragment of liprin-α2, as R194 is located at the middle of the H3-helix (Figure S1). Interestingly, the WT protein and the R194C mutant of H3 both form homotetramers (Figures 1C and S2C), indicating that H3 is capable of tetramerizing by itself and that R194 does not participate in H3 tetramerization. Because the H23 fragment undergoes dimer formation, H2 may inhibit H3 tetramerization. Thus, we analyzed the purified H2 fragment. However, the protein quality of H2 was poor, as indicated by analytical gel filtration (Figure S2D). Extensive trials of protein modification showed that either mutating C143 to an alanine (C143A) or removing the C-terminal sequence (H2ΔC) improved protein quality (Figures S2D and S2E). The MALS analysis indicated that H2-C143A has an average molecular weight close to the theoretical molecular weight of the H2 tetramer, while H2ΔC is likely to form dimers (Figures S2E and S2F).

Tetrameric coiled-coil structures of H2 and H3 in liprin-α2

After obtaining high-quality samples of the H2 and H3 fragments, we strove to determine their structures to discover their oligomerization and regulation mechanisms. By using X-ray crystallography, we successfully solved the liprin-α2_H3 structure at 1.7-Å resolution (Table 1). The crystal structure reveals that four H3 molecules in one asymmetric unit form two parallel coiled coils, which clamp with each other through their N termini in a head-to-head manner and fold as a homotetramer with a length of ~16 nm (Figures 1F and S1). R194 is solvent exposed and relatively far away from the tetramerization interface, explaining why the R194C mutation does not affect H3 tetramerization (Figure S2C). The H3 tetramerization interface is predominately composed of hydrophobic residues (Figure 1G). These residues are tightly packed together to form a hydrophobic core in which L177 is buried. Consistent with our structural finding, replacing L177 with a hydrophilic glutamine disrupted H3 tetramerization and drove H3 dimerization (Figure S2C).

Next, we crystallized the liprin-α2_H2ΔC fragment and determined the H2ΔC-C143A structure (Table 1). In agreement with the dimer formation of H2ΔC in solution, H2ΔC-C143A folds as a parallel coiled-coil dimer (Figure S2G). As the sidechain of residue C143 in the structure faces solvent (Figure S2H), the C143A mutation likely eliminates nonspecific disulfide bond formation and improves protein homogeneity. Interestingly, a crystal packing analysis indicated that the two dimeric coiled coils of H2ΔC pack weakly with each other through their C termini (Figure S2G). As only three residues of each H2ΔC molecule are involved in crystal packing (Figure S2I), the crystallographic tetramer of H2ΔC is unlikely to be stable in solution. Nevertheless, considering that the potential C-terminal extension of the helical conformation in the H2 fragment, the additional C-terminal interaction between two H2 dimers may stabilize the H2 tetramer. Indeed, by solving the crystal structure of H2 with the C143A mutation (Table 1), we found that H2 has an extended C-terminal helical structure and forms a homotetramer with a much larger tetramerization interface (Figures 1H, S1, and S2J). In contrast to the head-to-head tetramerization mode of H3, two parallel H2 coiled coils are clamped together in a tail-to-tail manner to form the H2 tetramer. Similar to the H3 tetramerization interface, the H2 tetramerization interface contains a number of hydrophobic residues that form a hydrophobic core (Figure 1I). Consistently, disrupting the hydrophobic interaction in H2 by introducing a hydrophilic mutation (L141Q) leads to the disruption of the H2 tetramer (Figure S2F). In addition to hydrophobic interactions, H2 tetramerization is further strengthened by salt bridges and hydrogen bonds (Figure 1I).

The R194C mutation impairs the intramolecular interaction between H2 and H3

Although the clamping directions of the dimeric coiled coils in the H2 and H3 tetramers are reversed, the core structures in the

Table 1. X-ray data collection and refinement statistics

Data collection	H3-SeMet	H3-native (PDB id: 7D2E)	H2ΔC-SeMet (PDB id: 7D2G)	H2-native (PDB id: 7D2H)
Space group	$P\,2_1$	$P\,2_1$	$C\,2$	$P\,2_1$
Cell dimensions				
a, b, c (Å)	37.141, 71.379, 53.981	38.307, 71.293, 53.473	126.057, 33.410, 73.631	32.879, 101.907, 37.445
α, β, γ (°)	90, 103.75, 90	90, 103.69, 90	90, 111.25, 90	90, 96.41, 90
Resolution (Å)	50–2.2 (2.24–2.2)	50–1.7 (1.73–1.7)	50–1.7 (1.76–1.7)	50–2.2 (2.24–2.2)
R_{merge}[a]	0.090 (0.887)	0.037 (0.757)	0.132 (1.312)	0.080 (0.847)
$I/\sigma I$	31.4 (3.6)	28.2 (1.9)	45.4 (2.0)	21.0 (1.6)
$CC_{1/2}$[b]	(0.872)	(0.744)	(0.902)	(0.753)
Completeness (%)	99.9 (100)	98.4 (99.5)	98.0 (92.4)	93.1 (94.3)
Redundancy	14.2 (14.2)	3.7 (3.7)	12.5 (9.6)	3.7 (3.6)
Refinement				
Resolution (Å)	–	50–1.7 (1.75–1.7)	50–1.7 (1.72–1.7)	50–2.2 (2.42–2.2)
No. reflections	–	30,253 (2,748)	31,588 (2,465)	11,539 (2,871)
R_{work} / R_{free}[c]	–	0.239 (0.332)/0.269 (0.334)	0.236 (0.384)/ 0.263 (0.430)	0.229 (0.343)/0.282 (0.408)
No. atoms				
Protein	–	1,993	1,625	1,840
Ligand/ion	–	0	6	6
Water	–	123	112	10
Mean B (Å)				
Protein	–	46.3	49.9	73.9
Ligand/ion	–	–	59.6	70.2
Water	–	45.4	53.0	69.4
Rmsds				
Bond lengths (Å)	–	0.006	0.002	0.001
Bond angles (°)	–	0.76	0.37	0.34
Ramachandran plot				
Favored region (%)	–	100	100	98.64
Allowed region (%)	–	0	0	1.36
Outliers (%)	–	0	0	0

The numbers in parentheses represent values for the highest-resolution shell.

$R_{free} = \Sigma_T||F_{obs}| - |F_{calc}||/\Sigma_T|F_{obs}|$, where T is a test dataset of about 4%–5% of the total reflections randomly chosen and set aside prior to refinement.

[a] $R_{merge} = \sum|I_i - I_m|/\sum I_i$, where I_i is the intensity of the measured reflection, and I_m is the mean intensity of all symmetry-related reflections.

[b] $CC_{1/2}$ is the correlation coefficient of the half datasets.

[c] $R_{work} = \Sigma||F_{obs}| - |F_{calc}||/\Sigma|F_{obs}|$, where F_{obs} and F_{calc} are observed and calculated structure factors.

four-helical coiled-coil regions of H2 and H3 are strikingly similar, as shown by the layered analysis of the tetramerization interface residues (Figures 1G and 1I). Specifically, the interactions among L141, L144, and V145 in the H2 tetramer highly resemble the interactions among L177, L174, and V173 in the H3 tetramer (layer 2 in Figure 1G and layer 4 in Figure 1I). Considering that the H23 fragment preferentially adopts the dimer conformation (Figure S2A), this structural observation prompted us to speculate that the dimeric H3 coiled coil may interact with the dimeric H2 coiled coil in head-to-tail binding mode, placing the N termini of the H3 dimer in close proximity to the C termini of the H2 dimer to enable the H2/H3 covalent connection in the CC1 (Figure 2A). In this H23 dimer, R194 is located very close to the C terminus of the H2 helix (Figure 2A). Given the negatively charged property of the helical C terminus, it is likely that the positively charged R194 interacts with the H2 C terminus via charge-charge attraction (Figure 2B). Together, we hypothesized that the intramolecular association between H2 and H3 stabilizes the H23 dimer and prevents either H2 or H3 from forming tetramers, whereas the R194C mutation destabilizes the H2/H3 interaction and thus drives both H2 and H3 tetramerization, resulting in CC1 oligomer formation (Figure 2C).

Consistent with our hypothesis, the isothermal titration calorimetry (ITC) analysis showed that H3 indeed binds to H2 with a K_d of ~17 μM (Figure 2D). Given that H2 covalently links with H3 in the full-length protein, this weak binding affinity is very likely sufficient to maintain the intramolecular H2/H3 interaction. However, the R194C mutation diminishes the binding of H3 to H2, as indicated by the ITC-based analysis (Figure 2D). Furthermore, the charged-reversed R194E mutant of H3 also disrupts H2 binding (Figure 2E) and shows an even higher potential to enhance the formation of tetramers and oligomers (Figure 2F), confirming a critical role for R194 in the H2/H3 interaction. In addition to the ITC-based analysis, the results from microscale thermophoresis (MST) experiments confirmed the importance of R194 for the H2/H3 interaction (Figure S2K). Although the binding of the R194C and R194E mutants of H3 to H2 was hardly detectable by ITC, the MST-based analysis showed that these H3 mutants still weakly associate (~100 μM) with H2, suggesting that the H2/H3 interaction involves not only the R194-mediated polar interaction, but also the hydrophobic interactions between the N termini of the H3 coiled coil and the C termini of the H2 coiled coil. Consistently, the dimer fraction of the R194C or R194E CC1 mutant remains ~30%–40% (Figures 1E and 2F), presumably due to the hydrophobic interactions between H3 and H2. The L177Q mutation disrupts the hydrophobic interactions in the H3 tetramerization interface (Figure S2C), according to our H23 dimer model (Figure 2A), which may also interfere with the H2/H3 interaction. As expected, L177Q largely decreased the dimer fraction of CC1 (Figure 2G). In contrast to the R194C mutant, despite disrupting the dimer formation, the L177Q mutant does not significantly increase the oligomer population, supporting the hypothesis that H3 tetramerization is essential for the formation of CC1 oligomers.

In liprin-α2, the CC1 is followed by a long, dimeric CC2 coiled coil (Figures 1A and S2L). To investigate whether the oligomeric dynamics of CC1 are affected by CC2, we purified and analyzed the CC12 fragment that contains both CC1 and CC2 (Figure 2H). As indicated by analytical gel filtration and MALS, CC12 mainly

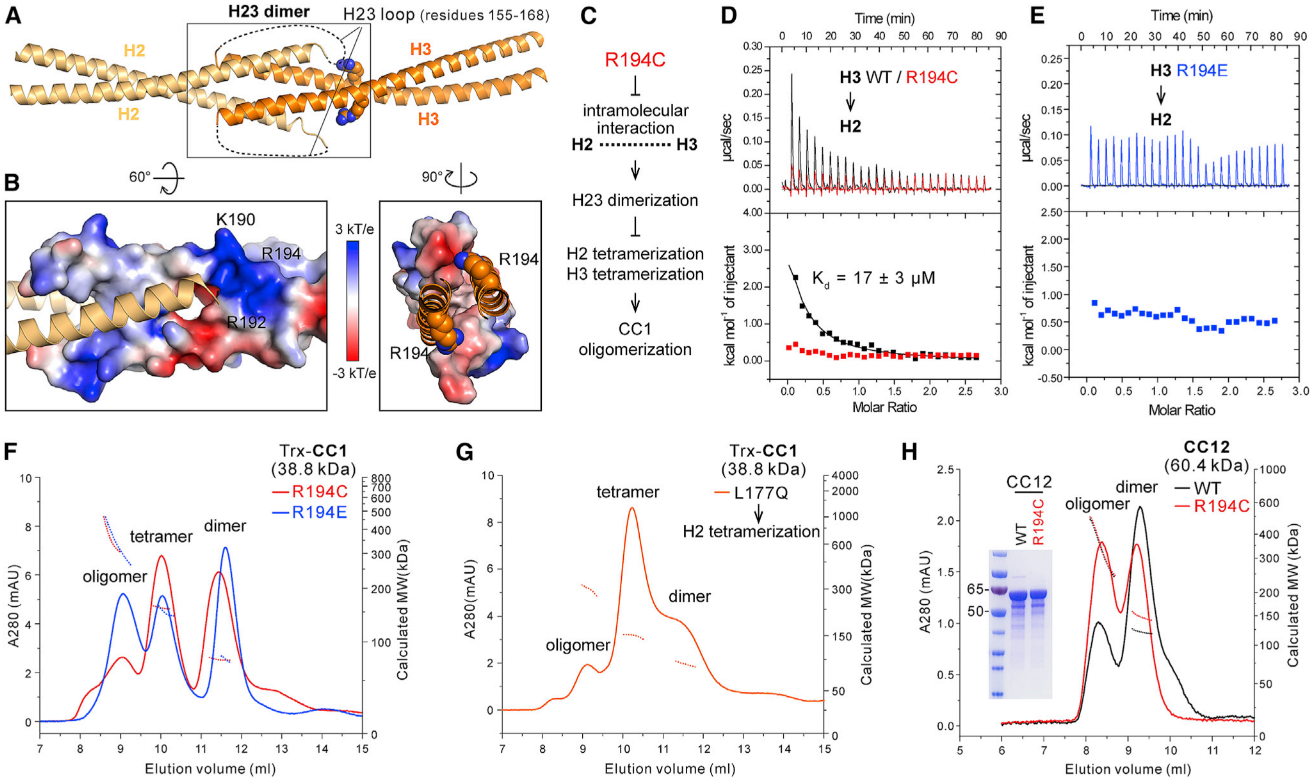

Figure 2. The R194C mutation disrupts the intramolecular interaction between the H2 and H3 fragments and promotes the oligomerization of liprin-α2_CC1

(A) Structural model of the H23 dimer. The loop connecting H2 and H3 is indicated by dashed lines.

(B) Charge potential analysis on the H3 (left panel) and H2 (right panel) surfaces. The negatively charged C termini of the H2 coiled coil closely contact the positively charged surface patch comprising K190, R192, and R194.

(C) Proposed mechanism for R194C-enhanced oligomerization of liprin-α2_CC1.

(D and E) ITC-based analysis of the H2/H3 interaction. The binding of H3 to H2 was disrupted by either R194C (D) or R194E (E) at the H3 fragment.

(F) Analytical gel filtration and MALS analysis showing the enhanced oligomerization of CC1 by the R194E mutation. The same analysis for the CC1-R194C mutant was also performed for comparison.

(G) Analytical gel filtration and MALS analysis of CC1-L177Q. The L177Q mutation reduced not only the tetramerization of H3, but also the dimerization of H23, resulting in the enhanced tetramerization of H2.

(H) Analytical gel filtration and MALS analysis of the CC12 fragment. Protein purity was checked by SDS-PAGE.

See also Figure S2.

forms dimers, while the CC12-R194C mutant forms a much higher level of oligomers, indicating that R194C-promoted oligomerization occurs in the N-terminal coiled-coil region of liprin-α2 and possibly in the full-length protein. In summary, our structural and biochemical analyses demonstrated that H2 and H3 interact with each other to form dimers of liprin-α2 and that the R194 mutation impairs the H2/H3 interaction to promote the switch from coiled-coil dimer formation to oligomer formation. Since the H2 C-terminal and H3 N-terminal regions are both strictly conserved in the liprin-α homologs from human to worms (Figure S1), the dimer-oligomer transition of liprin-α2 is very likely a common feature of all liprin-α proteins.

The coiled-coil region of liprin-α2 dynamically transitions between dimer and oligomer formation

The H23 fragment is the minimal region that undergoes the dimer-to-oligomer transition in liprin-α2 (Figure S2A). To understand the dynamics of the switching between dimer and tetramer/oligomer formation by H23, we carefully analyzed the different oligomeric states of H23 by separately collecting the dimer, tetramer, and oligomer fractions (Figure S3A) and rerunning these samples in a gel filtration column (Figure 3A). Interestingly, regardless of their initial oligomeric states, all three samples show a similar oligomeric distribution with the majority consisting of dimers, indicating that the dimeric conformation is thermodynamically favored and that the transition between different oligomeric states is relatively fast. In contrast, the R194C mutant of H23 shows very few transitions from tetramers/oligomers to dimers but a higher rate of transition from dimers to tetramers (Figure 3B), indicating that the R194C mutant changes the dynamic equilibrium between dimer and tetramer/oligomer by destabilizing the H23 dimer. Thus, we proposed that CC1 has an energetic preference for dimer formation through the R194-enhanced interaction between H2 and H3,

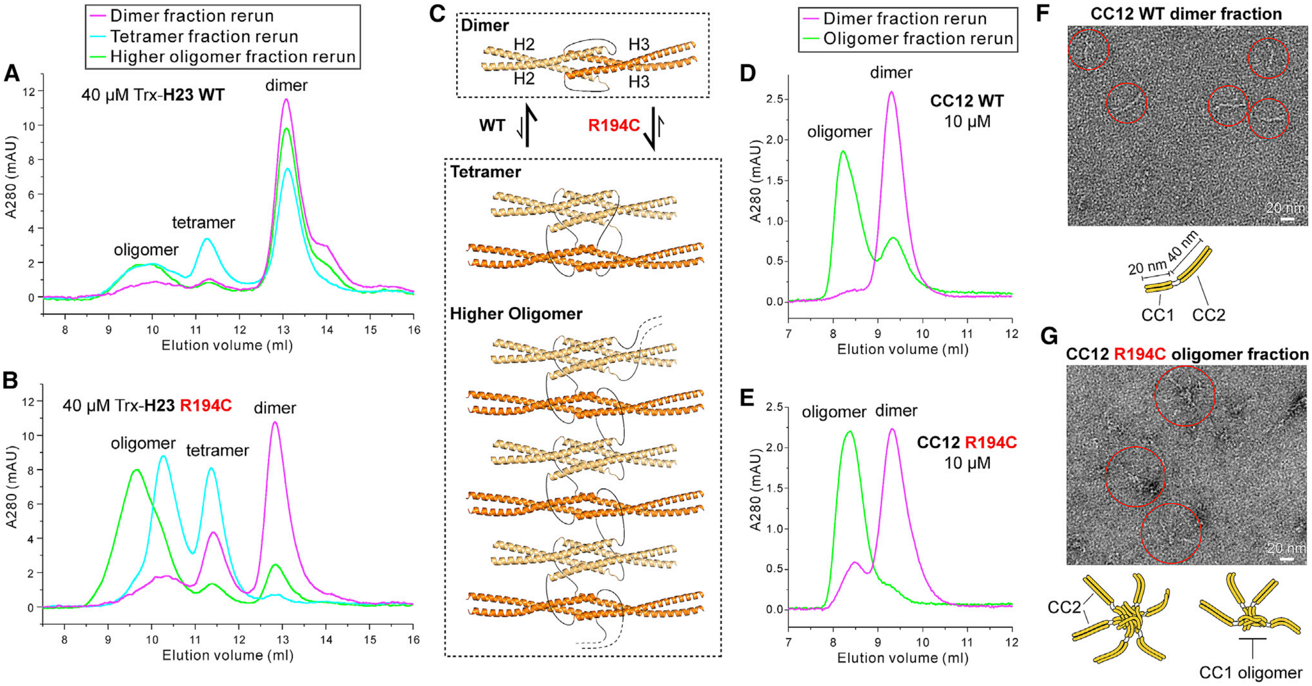

Figure 3. The R194C mutation enhances the dimer-to-oligomer transition of liprin-α2_CC12

(A and B) Dimer-to-oligomer transitions of Trx-tagged H23-WT (A) and R194C (B) were analyzed by separately harvesting the dimer, tetramer, and oligomer fractions and rerunning analytical gel filtration.

(C) Schematic model showing the different preferences of H23-WT and R194C for the transition between dimer and tetramer/oligomer.

(D and E) Dimer-to-oligomer transitions of CC12-WT (D) and R194C (E) were analyzed by separately harvesting the dimer and oligomer fractions (Figures S3A and S3B) and rerunning analytical gel filtration.

(F) EM analysis of the CC12 dimer prepared by negative staining. A schematic model of the CC12 dimer is indicated below.

(G) EM analysis of the CC12-R194C oligomer prepared by negative staining. Schematic models of the CC12 oligomers are indicated below.

See also Figure S3.

whereas the R194C mutation weakens the H2/H3 interaction, and thereby H2 and H3 tetramerization effectively competes with H23 dimerization, driving the formation of either tetramers or oligomers (Figure 3C).

To validate our proposed model, we performed the same dynamic property analysis with the entire coiled-coil region (CC12) of liprin-α2 (Figures 3D, 3E, and S3B). Although CC12 exhibits a slower dynamic exchange between the dimer and oligomer states, the R194C mutation significantly promotes the dimer-to-oligomer transition while inhibiting the opposite transition. Since CC12 has a molecular weight of ~60 kDa, the CC12 dimer or oligomer is suitable, size-wise, for EM analysis. Thus, we collected the dimeric and oligomeric fractions of CC12 and those of the R194C mutant and prepared EM samples with negative staining. As expected, we observed rod-like structures in the dimeric fractions of both the WT and R194C proteins (Figures 3F and S3C). Most of the rod-like structures were approximately 60 nm in length, equal to the total length of CC1 (~20 nm) and CC2 (~40 nm) when extended in coiled-coil dimers (Figure 3F). In contrast, most of the oligomeric R194C mutant of CC12 forms a particle with multiple tentacles with a length of ~40 nm (Figure 3G), which is similar to the extended length of CC2. Likewise, the oligomeric fraction of WT CC12 shows tentacled structures similar to those formed by the R194C mutant, although some rod-like particles were also observed (Figure S3D). The EM results indicate that CC1 forms a compact aggregate in the CC12 oligomer, supporting our model as shown in Figure 3C. The long CC2 coiled coils are toward the outside of this CC1 oligomer, making them accessible for recognition by presynaptic binding partners of liprin-α, such as ELKS and RIM (Ko et al., 2003; Schoch et al., 2002).

Oligomerized liprin-α2 promotes the LLPS of ELKS *in vitro* and in living cells

Studies with *C. elegans* have shown that liprin-α/SYD2 organizes the presynaptic active zone assembly by interacting with ELKS and that the gain-of-function mutation (R184C) in SYD2 facilitates the recruitment of ELKS to the presynaptic active zone (Dai et al., 2006), although the underlying mechanism is unknown. Mammalian ELKS homologs ELKS1 and ELKS2—each consisting of an N-terminal intrinsic disorder region (IDR), a long coiled-coil region, and a C-terminal Postsynaptic density-95/Discs large/Zona occludens-1 (PDZ)-binding motif (PBM) (Figures 4A, S4A, and S4B)—were reported to interact with liprin-αs via their N-terminal halves (Ko et al., 2003). Consistent with previous findings, in our coimmunoprecipitation (coIP) assay, the N-terminal segment of ELKS1 (ELKS1_N) or ELKS2 (ELKS2_N), consisting of the IDR and subsequent coiled coils,

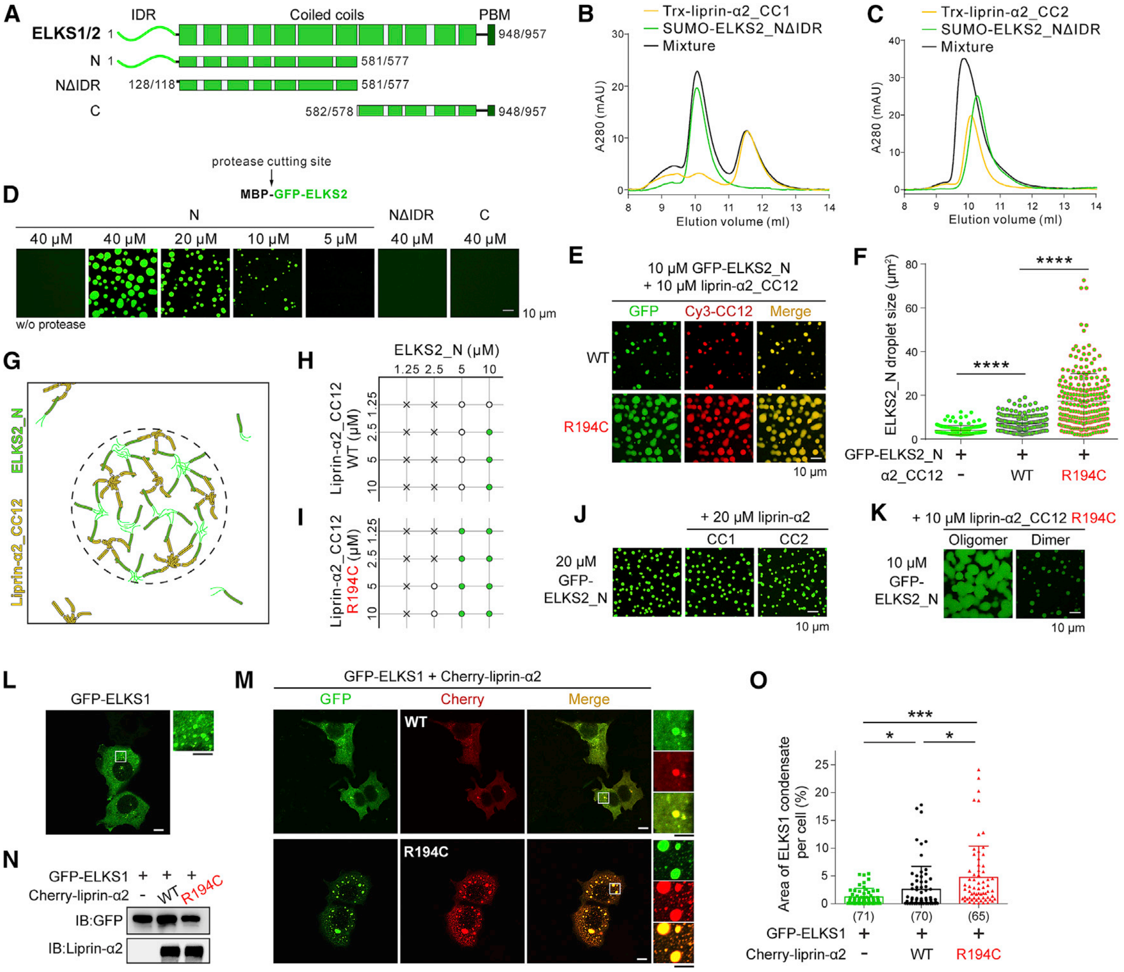

Figure 4. Oligomerized liprin-α2_CC12 promotes the LLPS of ELKS

(A) Cartoon diagrams of domain organizations of ELKS1 and ELKS2. The boundaries of different truncations are indicated by residues numbers.

(B and C) Analytical gel filtration analysis showing that no binding occurs between ELKS2_NΔIDR and liprin-α2_CC1 (B) while ELKS2_NΔIDR forms a complex with CC2 (C). Each protein has a concentration of 50 μM.

(D) Concentration-dependent LLPS of ELKS2. The MBP-tag was cleaved from the fusion proteins to induce LLPS.

(E) Confocal imaging of co-phase separation of ELKS2_N and liprin-α2_CC12.

(F) Quantification of the droplet sizes of ELKS2_N only shown in (D) (10 μM, n = 161 droplets examined over eight independent observation fields) and ELKS2_N/liprin-α2_CC12 shown in (E) (n = 186 and n = 227 droplets for WT and R194C, respectively). Data are shown as mean ± SD. ns, not significant; *$p < 0.05$, **$p < 0.01$, ***$p < 0.001$, and ****$p < 0.0001$ using unpaired Student's t test.

(G) A model depicting the involvement of oligomerized liprin-α2_CC12 in the LLPS of ELKS2_N via multivalent binding. The dashed circle indicates a condensed phase droplet filled with liprin-α2_CC12 and ELKS2_N.

(H and I) Summary plots of the concentration-dependent promotion of liprin-α2_CC12-WT (H) and R194C (I) on the LLPS of ELKS2_N. Corresponding confocal images are shown in Figures S5E and S5F. Open and closed circles indicate observation of subtle and obvious phase separations, respectively.

(J) Unchanged LLPS of ELKS2_N when adding either liprin-α2_CC1 or CC2.

(K) Confocal images showing the promotion effects of the liprin-α2_CC12-R194C oligomer and dimer on the LLPS of ELKS2_N.

(L and M) Cell imaging of overexpressed GFP-ELKS1 alone (L) or overexpressed GFP-ELKS1 and Cherry-liprin-α2 (M) in HEK293T cells, observed under a Nikon A1R confocal microscope. Scale bar, 10 μm. Regions of interest were highlighted by white boxes and enlarged to 4 times and aligned at the right of each merged image (scale bar, 5 μm).

(N) Western immunoblots of the transfected HEK293T cells shown in (L) and (M) using GFP and liprin-α2 antibodies. The overall expression levels for both GFP-ELKS1 and Cherry-liprin-α2 are comparable in different transfections.

(O) Quantification of the GFP-ELKS1 clustering levels as shown in (L) and (M). Data are presented as mean ± SD ~70 cells per experimental condition. The unpaired Student's t test analysis was used to define a statistically significant difference (*$p < 0.05$; **$p < 0.01$; ***$p < 0.001$).

See also Figures S4 and S5.

was sufficient to form a complex that contains liprin-α2 by overexpressing different boundaries of either ELKS1 or ELKS2 with liprin-α2 in HEK293T cells (Figures S4C and S4D). The N-terminal region of liprin-α, including CC1 and CC2, was found to be the ELKS-binding site (Ko et al., 2003). To dissect the region of liprin-α binding to ELKS, we analyzed the interaction between liprin-α2_CC1 or CC2 and the N-terminal coiled coils of ELKS2 without the IDR (ELKS2_NΔIDR) by using analytical gel filtration, as removing the IDR negligibly affects the binding of ELKS to liprin-α2 (Figures S4C and S4D). The results indicated that CC2, but not CC1, is required for the liprin-α2/ELKS interaction (Figures 4B and 4C).

The N-terminal region of ELKS was suggested to form cytoplasmic condensates through LLPS (Sala et al., 2019). To determine the essential element in ELKS for phase separation, we designed *in vitro* recombinant proteins of ELKS1/2 with a dual tag of maltose-binding protein (MBP) and green fluorescence protein (GFP) connected with a tobacco etch virus (TEV) protease cleavage site (Figure 4D) (Alberti et al., 2018; Fang et al., 2019). As the MBP tag increased the solubility of the fusion protein, the protein solution of MBP-GFP-tagged ELKS2_N was clear. However, after adding the TEV protease to remove the MBP tag, a large number of spherical droplets appeared in the GFP-ELKS2_N sample in a concentration-dependent manner (Figure 4D), confirming that ELKS2_N phase separates. Meanwhile, neither ELKS2_NΔIDR nor the C-terminal half of ELKS2 (ELKS2_C) showed condensate formation (Figure 4D), indicating that the IDR is required for the LLPS of ELKS2. Similar to the condensate formation observed for ELKS2, the N-terminal region of ELKS1 also underwent LLPS in an IDR-dependent manner (Figure S5A).

To determine the potential effect of liprin-α2 on the LLPS of ELKS2, we mixed Cy3-labeled liprin-α2_CC12 with GFP-ELKS2_N in a 1:1 ratio. Interestingly, the highly oligomerized R194C mutant not only co-phase separated with ELKS1_N and ELKS2_N, but also dramatically enlarged the droplets, while the WT CC12 showed slightly increased droplet size (Figures 4E, 4F, and S5B), although CC12 per se did not undergo phase separation (Figure S5C). Because the oligomerization of liprin-α2_CC12 generates multiple tentacles of CC2 for the binding of ELKS2 (Figure 3G) and ELKS2_NΔIDR forms a dimer in solution (Figure S5D), it is likely that the multivalent binding occurs between oligomeric liprin-α2 and dimeric ELKS2, which increases the LLPS capacity of ELKS2 (Figure 4G). A dose-dependent LLPS analysis confirmed the liprin-α2_CC12-mediated promotion of the ELKS2_N condensate, the concentration threshold of which decreased from 10 μM to below 5 μM (Figures 4H, 4I, S5E, and S5F). On the other hand, even at a concentration of 1.25 μM, the R194C mutant of CC12 had the potential for this promoting effect. In addition, neither CC1 nor CC2 alone enhanced the LLPS of ELKS2_N (Figure 4J). These results indicate that the promotion of the ELKS2 condensate requires both the oligomerization of liprin-α2 and the interaction between liprin-α2 and ELKS2. Consistently, adding the oligomer fraction of CC12-R194C boosted the LLPS of ELKS2_N, while adding the dimer fraction of CC12-R194C led to a weak promotion of the condensate at a level similar to that of the largely dimerized WT CC12 (Figure 4K).

Next, we tried to analyze the promoting effect of liprin-α2 on the LLPS of ELKS2 in living cells. However, the overexpressed full-length protein of ELKS2 was highly degraded in the cells (Figure S4D). Therefore, we chose ELKS1 for the cellular analysis. By overexpressing GFP-ELKS1 in HEK293T cells, we indeed observed small puncta of ELKS1 (Figure 4L). In support of the supposition that the LLPS of ELKS1/2 is promoted by the R194C-induced oligomerization of liprin-α2 in solution, ELKS1 and liprin-α2 formed large spherical co-condensates in the cells co-transfected with the R194C mutant of liprin-α2 (Figures 4M–4O). We then plotted the condensate area against the GFP-ELKS1 concentration indicated by GFP signal and confirmed that the condensate formation in these cells is concentration dependent, as the condensate area increased along with the GFP-ELKS1 level (Figure S5G). In addition, with the liprin-α2 overexpression, the concentration-dependent increase of the condensate was elevated. Even with a low level of GFP-ELKS1 expression in the cells, the condensate formation was significantly driven by co-expression with the R194C mutant (Figure S5H). As Cherry-liprin-α2 alone formed small puncta in the transfected HEK293T cells (Figure S5I), it is possible that liprin-α2 also phase-separates through a region other than CC12 to promote ELKS1 LLPS. Consistently, recent LLPS studies have reported that liprin-α3 and SYD2 undergo phase separation through the largely unstructured region connecting CC12 and three C-terminal SAM domains (Emperador-Melero et al., 2020; McDonald et al., 2020). Nevertheless, the cellular observations of larger spherical condensates formed by the R194C mutant (Figures S5I and S5J) and the decreased condensate formation of liprin-α2 by deleting CC1 (Figure S5K) indicate that the oligomerization of CC1 is important for the condensate formation of liprin-α2. Taken together, our above LLPS analysis suggested that liprin-α2 can promote the LLPS of ELKS1/2 via oligomerization to increase the binding valency (Figure 4G) and to facilitate protein assembly.

The involvement of liprin-α2 decreases the ELKS2 concentration in droplets and alters LLPS dynamics

We employed an *in vitro* sedimentation-based assay to confirm the promotion effect of liprin-α2 on the LLPS of ELKS2. Surprisingly, the overall amount of ELKS2_N undergoing LLPS only slightly increased after the addition of CC12-R194C and did not increase with increasing amounts of CC12-R194C in the bulk solution or the pellets (Figures 5A and 5B), contrasting the massive increase in size and number of droplets induced by CC12-R194C (Figures 4E and S5F). Interestingly, the confocal imaging analysis revealed that the fluorescence signal of GFP-ELKS2_N in the droplet became weaker after CC12 or its R194C mutant was added (Figures 5C and 5D) and was further decreased with the amount of CC12-R194C increased in the mixture (Figure S6A). By measuring the ELKS2_N and liprin-α2_CC12 concentrations in the condensate with a fluorescence-imaging-based assay (Wu et al., 2019), we found that both proteins were highly concentrated (~1–2 mM) in the droplet (Figures 5E, S6B, and S6C) and that the ELKS2_N concentration in droplets was dependent on the initial CC12/ELKS2_N mixing ratio (Figure S6D). These results indicate that liprin-α2_CC12 decreases the requirement for the ELKS2_N scaffolds in phase

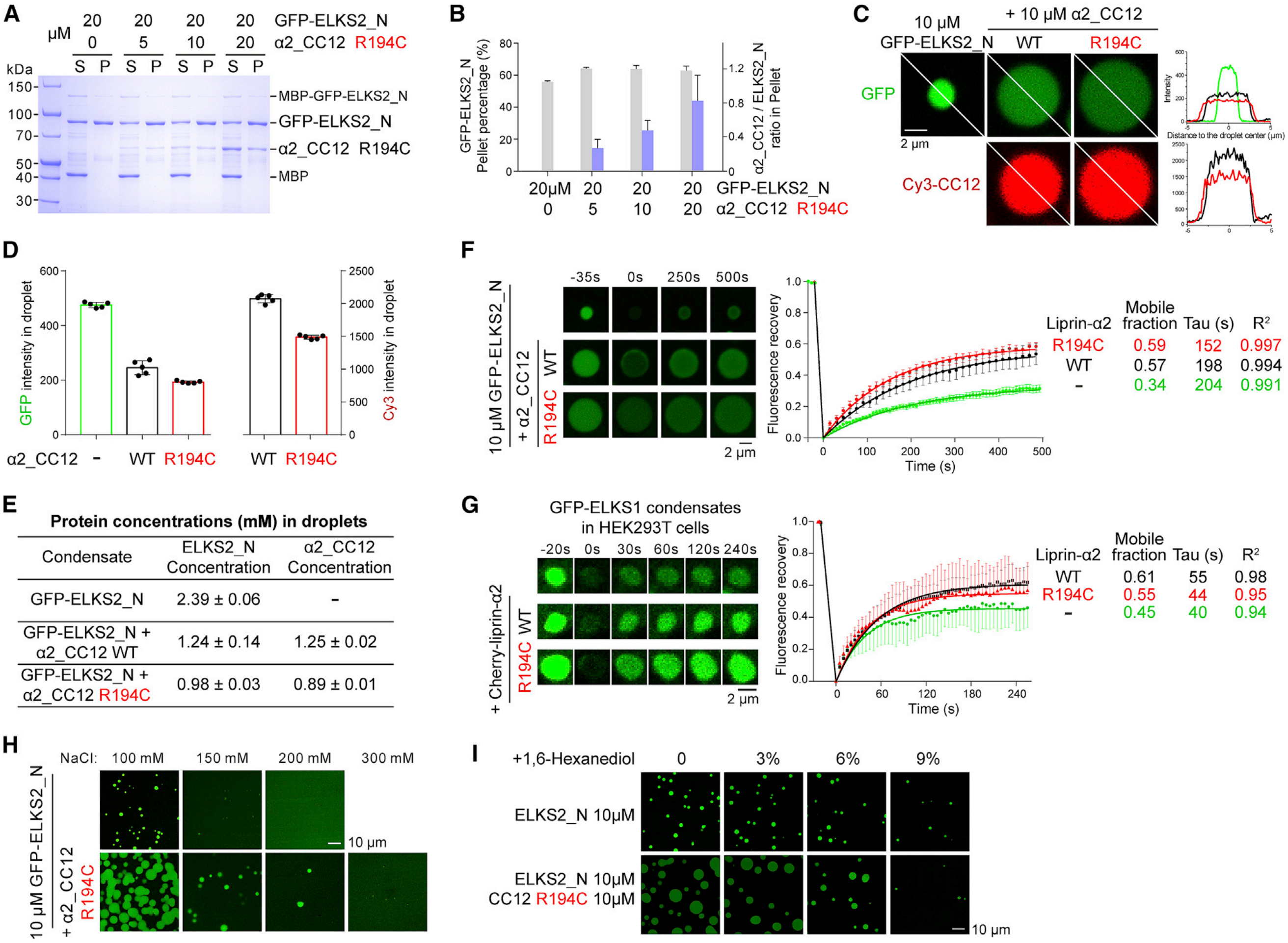

E

Protein concentrations (mM) in droplets

Condensate	ELKS2_N Concentration	α2_CC12 Concentration
GFP-ELKS2_N	2.39 ± 0.06	-
GFP-ELKS2_N + α2_CC12 WT	1.24 ± 0.14	1.25 ± 0.02
GFP-ELKS2_N + α2_CC12 R194C	0.98 ± 0.03	0.89 ± 0.01

Figure 5. Liprin-α2_CC12 alters the scaffolding of the ELKS LLPS

(A) Sedimentation-based assay indicating the distributions of GFP-ELKS2_N in supernatant (S) and pellet (P) when mixed with different concentrations of liprin-α2_CC12 R194C. The MBP-GFP tagged ELKS2_N were treated by TEV protease after mixing.

(B) Quantification of the pellet percentages of GFP-ELKS2_N and the molar ratio of liprin-α2_CC12/ELKS_N in pellet in the samples shown in (A). The results are expressed as mean ± SD, with results from three independent batches of sedimentation experiments.

(C) Confocal imaging of ELKS2 droplets in different conditions and corresponding line analysis of the GFP and Cy3 intensities across the droplets. Curves are colored in green, black, and red for GFP-ELKS2_N, GFP-ELKS2_N plus CC12, and GFP-ELKS2_N plus CC12-R194C, respectively. The color coding is also applied to other panels. The starting concentration for all three proteins in the mixture was 10 μM. The liprin-α2_CC12 samples contains 5% Cy3-labeled proteins.

(D) Quantification of GFP and Cy3 intensities shown in (C). Intensity values were collected from five droplets in each group and are presented as mean ± SD.

(E) Summary table of the protein concentrations calculated based on the standard curves and fluorescent intensities shown in Figures S6B and S6C. Values are presented as mean ± SD from three independent batches of experiments.

(F) *In vitro* FRAP analysis of the dynamics of the ELKS2_N molecules in the droplets. Each averaged signal is from eight droplets, and data are presented as mean ± SD. The data were fitted by using one-phase exponential association.

(G) FRAP experiments in HEK293T cells transfected with GFP-ELKS1 with or without exogenous expressed Cherry-liprin-α2 in HEK293T cells. Recovery curves of GFP-ELKS1 condensates are shown in the right panel. Each averaged signal is from eight cells, and data are presented as mean ± SD.

(H) Salt disruption on phase separation of ELKS2_N with or without CC12 R194C.

(I) 1,6-Hexanediol disruption on the ELKS2_N condensate with or without CC12-R194C.

See also Figure S6.

formation, presumably due to the involvement of liprin-α2_CC12 in the scaffolding of the ELKS2_N LLPS. Hence, the decreased ELKS2_N concentration in the droplet offsets the increased droplet volume of ELKS2_N when highly oligomerized CC12 was added.

In addition, the involvement of liprin-α2_CC12 in the LLPS accelerates the dynamic exchange of the ELKS2 molecule between condensed phase and aqueous solution both *in vitro* and in living cells, as indicated by the increased mobile fraction in the fluorescence recovery after photobleaching (FRAP) experiments (Figures 5F and 5G). This outcome suggests that the IDR-mediated LLPS of ELKS2 is less dynamic than the LLPS involving the multivalent interaction between liprin-α2 and ELKS2. Although the capability of the WT CC12 to form oligomers is much weaker than that of the R194C mutant (Figure S3B), the highly concentrated WT CC12 (~1 mM) in the ELKS2_N droplet may drive the oligomerization of CC12 and thereby result in altered ELKS2_N dynamics similar to those caused by CC12-R194C. Furthermore, the LLPS of ELKS2_N alone was either largely diminished or abolished in a buffer with salt concentrations higher than 100 mM, whereas ELKS2_N and CC12 continued to form relatively large droplets under 200-mM salt conditions (Figure 5H), implying that the multivalent interaction contributes to the scaffolding stability of LLPS. On the other hand, the ELKS2_N/liprin-α2_CC12 droplets became smaller or even disappeared when treated with the increased 1,6-hexanediol concentration (Figure 5I). In contrast, the 1,6-hexanediol-induced reduction of the droplet size was modest for ELKS2_N LLPS without liprin-α2_CC12 (Figures 5I and S6E). As 1,6-hexanediol can dissolve liquid-like condensates rather than gel-/solid-like condensates (Kroschwald et al., 2017), it is likely that ELKS2_N forms the condensates having a hydrogel-like property and that the involvement of liprin-α2_CC12 in the ELKS2_N condensate alters the organization of ELKS2_N molecules and converts the condensate to be more liquid-like.

Together, our LLPS analysis demonstrated that by binding to ELKS, liprin-α2 acts as an additional scaffolding molecule during LLPS to promote and reorganize protein assembly (Figure 4G). Given the important roles of ELKS in active zone formation, our results suggested that the liprin-α oligomer enhances the accumulation of ELKS in the active zone (Dai et al., 2006; Kittelmann et al., 2013) by significantly decreasing the concentration threshold for the condensate formation of ELKS.

Liprin-α2 drives ELKS2 to induce high concentrations of RIM1α in the condensed phase

Since RIM and RIM-BP (RBP), two other active zone scaffolds, were found to co-phase separate and cluster voltage-gated Ca^{2+} channels (VGCCs) (Wu et al., 2019), an intriguing question is raised: how does the LLPS of ELKS coexist with the LLPS of RIM and RBP within the active zone, regarding that both liprin-α and ELKS can interact with RIM (Ko et al., 2003; Schoch et al., 2002)? To address this question, we first reproduced the RIM1α/RBP2 condensate using purified RIM1α and RBP2_(SH3)$_3$ proteins (Figures 6A and S7A). As ELKS binds to the PDZ domain of RIM through the PBM at its C terminus (Ohtsuka et al., 2002; Wang et al., 2002), we fused the PBM sequence to the C terminus of ELKS2_N to generate ELKS2_NPBM (Figure 6A). Similar to ELKS2_N, ELKS2_NPBM showed the capacity for LLPS and underwent enhanced phase separation with liprin-α2_CC12-R194C (Figures S7B–S7E). To exclude the potential influence of the ELKS2_NPBM LLPS on the recruitment of ELKS2_NPBM to the RIM1α/RBP2 droplet, we used highly soluble MBP-GFP-ELKS2_NPBM in the LLPS assay. We found that the fusion protein accumulated in the RIM1α/RBP2 droplets without significantly affecting LLPS dynamics, and deleting the last four residues (ΔGIWA) required for RIM binding abolished this enrichment (Figures 6B and S7F), indicating that ELKS2 can be specifically recruited to the RIM1α/RBP2 condensate via the PBM/PDZ interaction. In contrast, although liprin-α2_CC2 binds to the C2B domain of RIM1α (Figure S7G), both WT CC12 and CC12-R194C failed to accumulate at the RIM1α/RBP2 condensate (Figure 6B), implying that the condensed phase provides an environment different from that in the aqueous solution for protein-protein interactions.

Next, we mixed the RIM1α/RBP2 condensate with the ELKS2/liprin-α2 condensate. Surprisingly, these two protein condensates remained mutually exclusive (Figure 6C), even though RIM1α can form a complex with both liprin-α2 and ELKS2 in solution (Figure S7H). Interestingly, we observed that RIM1α was highly enriched in the ELKS2_NPBM/CC12-R194C droplets with a concentration even higher than that in the RIM1α/RBP2 droplets (Figure 6C). This enrichment requires the binding of RIM1α to ELKS2, as little RIM1α accumulation was found in the ELKS2_NPBM-ΔGIWA/CC12-R194C droplets (Figure 6C). To determine the role of liprin-α2_CC12 in the maintenance of this exclusion of the two condensates, we analyzed the interplay between droplets when the RIM1α/RBP2 droplets were added to the solution containing either the ELKS2_NPBM droplets or the ELKS2_NPBM/CC12-R194C droplets. As expected, the ELKS2_NPBM droplet quickly fused with the RIM1α/RBP2 droplets (Figure 6D; Video S1), whereas the presence of CC12-R194C in the LLPS of ELKS2_NPBM not only blocked this droplet fusion, but also prevented ELKS2_NPBM from entering the RIM1α/RBP2 condensate (Figure 6E; Video S2). In addition, the difference of the RIM1α distribution in the two condensates was increased when CC12-R194C was added (Figures 6F and 6G). Given that the concentration of RIM1α remained at the same level in the RIM1α/RBP2 droplets, our observation indicates that the enrichment of RIM1α in the LLPS of ELKS2_NPBM can be further enhanced by oligomerized liprin-α2_CC12. Taken together, these LLPS data show that liprin-α2_CC12 controls the interplay between the two condensates by restricting the diffusion of ELKS2 into the RIM1α/RBP2 condensate and altering the ELKS2 assembly to accommodate more RIM1α molecules in the ELKS2 condensate.

RIM1α in the ELKS2_NPBM condensate loses the capability to assemble VGCCs

The LLPS of RIM1α and RBP2 can enrich the cytoplasmic tail of the N-type VGCC α1 subunit (NCav_CT) via the binding of NCav_CT to the PDZ domain of RIM and the SH3 domains of RIM-BP (Figure 6A) (Hibino et al., 2002; Kaeser et al., 2011; Wu et al., 2019). In line with previous findings, NCav_CT quickly entered and accumulated in the RIM1α droplets (Figure S7I), and the process was accelerated by the addition of RBP2_(SH3)$_3$ (Figure S7J). In contrast, mixing ELKS2_NPBM with RIM1α largely diminished the recruitment of NCav_CT to the condensed phase (Figure S7K). Considering that ELKS also interacts with the PDZ domain of RIM (Ohtsuka et al., 2002; Wang et al., 2002), it is very likely that ELKS2_NPBM competes with NCav_CT for binding to RIM1α, preventing NCav_CT from associating with RIM1α in the ELKS2 condensate. Since liprin-α2 regulates the enrichment of RIM1α in the ELKS2 condensate, we analyzed the effect of liprin-α2 on the distribution of NCav_CT by adding the NCav_CT protein to a mixture of the RIM1α/RBP2 condensate and the ELKS2/liprin-α2 condensate (Figure 6H). Again, NCav_CT was enriched only in the RIM1α/RBP2 condensate and not in the ELKS2_NPBM/liprin-α2 condensate (Figure 6H), even though the enrichment of RIM1α was much greater in the ELKS2_NPBM/liprin-α2

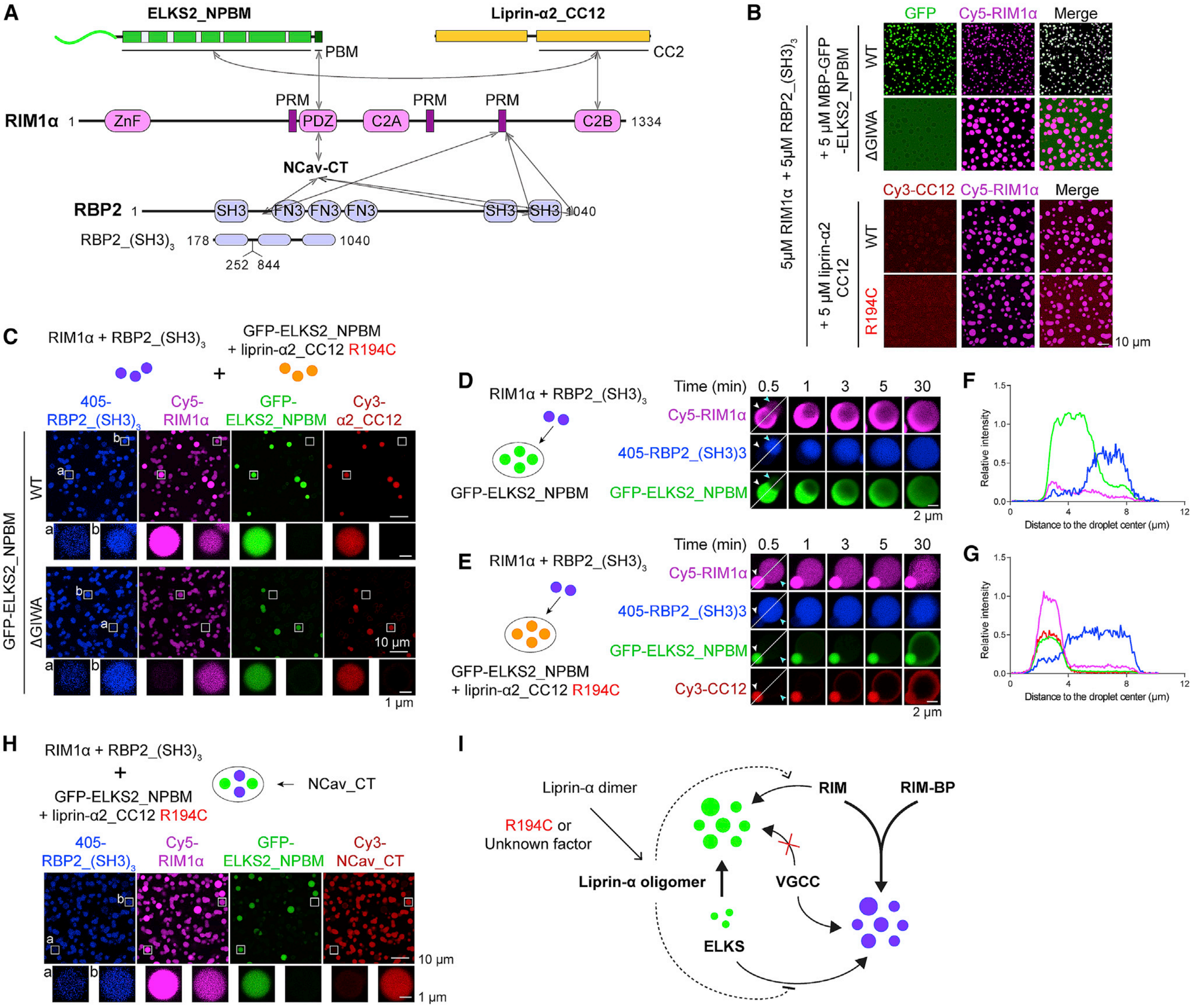

Figure 6. The distributions of RIM1α and NCav_CT in the condensed phases controlled by oligomerized liprin-α2_CC12

(A) Schematic diagram of the interaction network involving ELKS2_NPBM, liprin-α2_CC12, RIM1α, RBP2, and NCav-CT.

(B) The different enrichment of ELKS2 and liprin-α2_CC12-R194C at the RIM1α /RBP2 condensate. ELKS2_NPBM carrying the deletion of the last four residues (ΔGIWA) failed to be recruited to the droplets, while CC12-R194C showed very little enrichment at the condensed phase. The MBP tag was not cleaved to keep the ELKS2_NPBM protein in the highly soluble form.

(C) Confocal imaging analysis of the LLPS mixture of the RIM1α/RBP2_(SH3)$_3$ condensate and the ELKS2_NPBM/liprin-α2_CC12-R194C. White boxes labeled with "a" and "b" indicate the representative droplets of ELKS2_NPBM/liprin-α2_CC12-R194C and RIM1α/RBP2_(SH3)$_3$, respectively, which are shown below as zoom-in views. The concentration of each protein was 5 μM.

(D) Time-lapse snapshots of the fusion event occurring between the RIM1α/RBP2_(SH3)$_3$ droplet and the ELKS2_NPBM droplet. Except for ELKS2_NPBM (10 μM), the concentration of each protein was 5 μM.

(E) Time-lapse snapshots of the two closely attached droplets of RIM1α/RBP2_(SH3)$_3$ and ELKS2_NPBM/liprin-α2_CC12-R194C. The concentration of each protein was 5 μM.

(F) Line analysis of fluorescent intensities recorded at 0.5 min after mixing as shown in (D).

(G) Line analysis of fluorescent intensities recorded at 0.5 min after mixing as shown in (E).

(H) Confocal imaging analysis indicating the distinct distribution of NCav_CT in the RIM1α/RBP2_(SH3)$_3$ and ELKS2_NPBM/liprin-α2_CC12-R194C condensates. Images were recorded 25 min after adding 5 μM NCav_CT into the mixtures of the two condensates. The representative droplets of ELKS2_NPBM/liprin-α2_CC12-R194C and RIM1α/RBP2_(SH3)$_3$ are indicated by white boxes labeled with "a" and "b," respectively, and are further shown below as zoom-in views.

(I) Cartoon model depicting the multiple roles of liprin-α2 in regulating differential assembly of active zone proteins.

See also Figure S7 and Videos S1 and S2.

condensate. Thus, the distinct distributions of NCav_CT at the two different RIM1α-enriched condensates imply that liprin-α proteins interplay with ELKS and RIM-BP proteins to regulate the assembly and function of RIM at the active zone (Figure 6I).

DISCUSSION

The presynaptic active zone is composed of several interacting protein complexes, which are distributed in specific patterns to generate functional compartments (Emperador-Melero and Kaeser, 2020). How these patterns are constituted and maintained in the active zone remains enigmatic. In this study, we showed that liprin-α2, through its N-terminal coiled-coil region, participates in the LLPS-mediated assembly of ELKS proteins (Figure 4). In the absence of liprin-α2, ELKS2 can form co-condensates with RIM and RIM-BP via LLPS (Figure 6D). However, in the presence of liprin-α2, ELKS2 was not enriched in the RIM/RIM-BP condensate, while the RIM protein was highly concentrated in the ELKS2 condensate (Figures 6C and 6E). The different protein distributions result in the two different sets of protein assemblies: liprin-α/ELKS/RIM and RIM/RIM-BP, respectively. Consequently, VGCCs are specifically recruited to the condensates formed by the RIM/RIM-BP complex (Figure 6H). Therefore, the different protein assemblies presumably provide the scaffolding platform necessary to generate patterned structures with functional modules for the active zone. Importantly, liprin-α acts as a key regulator of this protein patterning by limiting the enrichment of ELKS in the assembly of RIM/RIM-BP and enhancing the accumulation of RIM in the condensed phase of ELKS (Figure 6I).

The regulatory role of liprin-α is achieved through the dimer-to-oligomer transition. By studying the R194C mutant of liprin-α2, we confirmed the R194C-enhanced self-oligomerization of liprin-α. However, the CC1-mediated oligomerization of liprin-α proteins under physiological conditions is triggered by an unknown factor or factors (Figure 6I). A plausible candidate is SYD1, which serves as an upstream regulator of liprin-α/SYD2 in synaptogenesis (Dai et al., 2006) and directly interacts with liprin-α (Wentzel et al., 2013). Whether the SYD1-binding can enhance the self-assembly of liprin-α requires further investigation. Considering that liprin-α and LAR function together to define the ultrastructure of the active zone (Kaufmann et al., 2002; Stryker and Johnson, 2007), the binding of liprin-α to LAR is another promising way for the assembly of liprin-α, as overexpressing LAR and liprin-α2 in COS7 cells robustly promoted not only LAR clustering on the plasma membrane, but also the accumulation of liprin-α2 in a liprin-α2/LAR-interaction-dependent manner (Xie et al., 2020).

Although electron-dense active zones exist in all synapses, their morphologies and molecular compositions vary in different types of neurons (Südhof, 2012). The protein ratios of ELKS and SYD1 were found to differentially position Munc13 isoforms at the active zone and thereby regulate functional diversity across synapses in different brain regions of *Drosophila* (Fulterer et al., 2018). Interestingly, we observed that liprin-α2_CC12 decreased the ELKS2_N concentration in the condensed phase (Figures 5C–5E) and that the ratio of the liprin-α2 and ELKS2 fragments determined the extent of the decrease (Figures S6A and S6D). It is tempting to speculate that the amount of ELKS protein at the active zone is largely decreased by oligomerized liprin-α, in which SYD1 indirectly controls the ELKS level through liprin-α and compartmentalizes the differential assembly of the Munc13 isoforms.

The LLPS of ELKS requires the IDR (Figures 4D and S5A), which is a typical element found in mediating LLPS (Alberti et al., 2019). However, the IDR of ELKS alone is insufficient for condensate formation in cells (Sala et al., 2019), suggesting that the N-terminal coiled-coil domain of ELKS contributes to LLPS. In addition, the coiled-coil domain of liprin-α promotes the LLPS of ELKS by forming the oligomerized coiled-coil structure (Figures 3C and 4G), largely increasing the binding valence for LLPS. Emerging studies on coiled-coil-containing proteins have revealed their capacity for LLPS (Fang et al., 2019; Lu et al., 2020; Zeng et al., 2016; Zhu et al., 2020). Considering that a large number of coiled-coil-containing proteins have been identified (Burkhard et al., 2001), coiled-coil-mediated/promoted LLPS is likely a common way to control protein assembly in various biological systems.

STAR★METHODS

Detailed methods are provided in the online version of this paper and include the following:

- KEY RESOURCES TABLE
- RESOURCE AVAILABILITY
  - ○ Lead contact
  - ○ Materials availability
  - ○ Data and code availability
- EXPERIMENTAL MODEL AND SUBJECT DETAILS
  - ○ HEK293T cells culture
  - ○ Bacterial strain
- METHOD DETAILS
  - ○ Expression constructs and site-directed mutagenesis
  - ○ Protein preparation
  - ○ Protein fluorescence labeling
  - ○ Analytical gel filtration chromatography
  - ○ Multi-angle light scattering (MALS) analysis
  - ○ Crystallography
  - ○ Structure determination and analysis
  - ○ Isothermal titration calorimetry (ITC) analysis
  - ○ Microscale thermophoresis (MST) analysis
  - ○ Negative staining and electron microscopy
  - ○ Co-immunoprecipitation and immunoblotting
  - ○ LLPS assays
  - ○ Protein concentration measurements in the condensed phase
  - ○ Fluorescence recovery after photo-bleaching assay (FRAP)
  - ○ Cell **culture, transfection and fluorescence** imaging
- QUANTIFICATION AND STATISTICAL ANALYSIS

SUPPLEMENTAL INFORMATION

Supplemental information can be found online at https://doi.org/10.1016/j.celrep.2021.108901.

ACKNOWLEDGMENTS

We thank Prof. Mingjie Zhang and Prof. Pilong Li for kindly providing plasmids. We also thank the assistance of Southern University of Science and Technology (SUSTech) Core Research Facilities and BL17U, BL18U, and BL19U1 beamlines of Shanghai Synchrotron Radiation Facility for data collection. This work was supported by the National Natural Science Foundation of China (grants 31971131 and 31770791 to Z.W. and 31870757 to C.Y.); the Natural Science Foundation of Guangdong Province (2016A030312016); Shenzhen-Hong Kong Institute of Brain Science, Shenzhen Fundamental Research Institutions (2021SHIBS0002); and Shenzhen Science and Technology Innovation Commission (JCYJ20170817105752394).

AUTHOR CONTRIBUTIONS

Z.W. conceived the study. Z.W. and C.Y. co-supervised the project. M.L., G.J., and X.X. designed experiments. M.L., G.J., and K.L. purified proteins and performed biochemistry assays. M.L. and Z.W. solved and analyzed structures. M.L. and F.N. performed EM experiments. X.X. and W.Z. performed coIP experiments and cellular assays. Z.W. and C.Y. wrote the manuscript with input from all authors.

DECLARATION OF INTERESTS

The authors declare no competing interests.

Received: October 19, 2020
Revised: February 2, 2021
Accepted: March 3, 2021
Published: March 23, 2021

REFERENCES

Ackley, B.D., Harrington, R.J., Hudson, M.L., Williams, L., Kenyon, C.J., Chisholm, A.D., and Jin, Y. (2005). The two isoforms of the Caenorhabditis elegans leukocyte-common antigen related receptor tyrosine phosphatase PTP-3 function independently in axon guidance and synapse formation. J. Neurosci. *25*, 7517–7528.

Acuna, C., Liu, X., and Südhof, T.C. (2016). How to Make an Active Zone: Unexpected Universal Functional Redundancy between RIMs and RIM-BPs. Neuron *91*, 792–807.

Adams, P.D., Afonine, P.V., Bunkóczi, G., Chen, V.B., Davis, I.W., Echols, N., Headd, J.J., Hung, L.W., Kapral, G.J., Grosse-Kunstleve, R.W., et al. (2010). PHENIX: a comprehensive Python-based system for macromolecular structure solution. Acta Crystallogr. D Biol. Crystallogr. *66*, 213–221.

Alberti, S., Saha, S., Woodruff, J.B., Franzmann, T.M., Wang, J., and Hyman, A.A. (2018). A User's Guide for Phase Separation Assays with Purified Proteins. J. Mol. Biol. *430*, 4806–4820.

Alberti, S., Gladfelter, A., and Mittag, T. (2019). Considerations and Challenges in Studying Liquid-Liquid Phase Separation and Biomolecular Condensates. Cell *176*, 419–434.

Biederer, T., Kaeser, P.S., and Blanpied, T.A. (2017). Transcellular Nanoalignment of Synaptic Function. Neuron *96*, 680–696.

Böhme, M.A., Beis, C., Reddy-Alla, S., Reynolds, E., Mampell, M.M., Grasskamp, A.T., Lützkendorf, J., Bergeron, D.D., Driller, J.H., Babikir, H., et al. (2016). Active zone scaffolds differentially accumulate Unc13 isoforms to tune Ca(2+) channel-vesicle coupling. Nat. Neurosci. *19*, 1311–1320.

Burkhard, P., Stetefeld, J., and Strelkov, S.V. (2001). Coiled coils: a highly versatile protein folding motif. Trends Cell Biol. *11*, 82–88.

Dai, Y., Taru, H., Deken, S.L., Grill, B., Ackley, B., Nonet, M.L., and Jin, Y. (2006). SYD-2 Liprin-alpha organizes presynaptic active zone formation through ELKS. Nat. Neurosci. *9*, 1479–1487.

Davis, I.W., Leaver-Fay, A., Chen, V.B., Block, J.N., Kapral, G.J., Wang, X., Murray, L.W., Arendall, W.B., 3rd, Snoeyink, J., Richardson, J.S., and Richardson, D.C. (2007). MolProbity: all-atom contacts and structure validation for proteins and nucleic acids. Nucleic Acids Res. *35*, W375-83.

Emperador-Melero, J., and Kaeser, P.S. (2020). Assembly of the presynaptic active zone. Curr. Opin. Neurobiol. *63*, 95–103.

Emperador-Melero, J., Wong, M.Y., Wang, S.S.H., De Nola, G., Kirchhausen, T., and Kaeser, P.S. (2020). Phosphorylation triggers presynaptic phase separation of Liprin-α3 to control active zone structure. BioRxiv.

Emsley, P., and Cowtan, K. (2004). Coot: model-building tools for molecular graphics. Acta Crystallogr. D Biol. Crystallogr. *60*, 2126–2132.

Fang, X., Wang, L., Ishikawa, R., Li, Y., Fiedler, M., Liu, F., Calder, G., Rowan, B., Weigel, D., Li, P., and Dean, C. (2019). Arabidopsis FLL2 promotes liquid-liquid phase separation of polyadenylation complexes. Nature *569*, 265–269.

Fulterer, A., Andlauer, T.F.M., Ender, A., Maglione, M., Eyring, K., Woitkuhn, J., Lehmann, M., Matkovic-Rachid, T., Geiger, J.R.P., Walter, A.M., et al. (2018). Active Zone Scaffold Protein Ratios Tune Functional Diversity across Brain Synapses. Cell Rep. *23*, 1259–1274.

Hibino, H., Pironkova, R., Onwumere, O., Vologodskaia, M., Hudspeth, A.J., and Lesage, F. (2002). RIM binding proteins (RBPs) couple Rab3-interacting molecules (RIMs) to voltage-gated Ca(2+) channels. Neuron *34*, 411–423.

Kaeser, P.S., Deng, L., Wang, Y., Dulubova, I., Liu, X., Rizo, J., and Südhof, T.C. (2011). RIM proteins tether Ca2+ channels to presynaptic active zones via a direct PDZ-domain interaction. Cell *144*, 282–295.

Kaufmann, N., DeProto, J., Ranjan, R., Wan, H., and Van Vactor, D. (2002). Drosophila liprin-alpha and the receptor phosphatase Dlar control synapse morphogenesis. Neuron *34*, 27–38.

Kittelmann, M., Hegermann, J., Goncharov, A., Taru, H., Ellisman, M.H., Richmond, J.E., Jin, Y., and Eimer, S. (2013). Liprin-α/SYD-2 determines the size of dense projections in presynaptic active zones in C. elegans. J. Cell Biol. *203*, 849–863.

Ko, J., Na, M., Kim, S., Lee, J.-R.R., and Kim, E. (2003). Interaction of the ERC family of RIM-binding proteins with the liprin-alpha family of multidomain proteins. J. Biol. Chem. *278*, 42377–42385.

Kroschwald, S., Maharana, S., and Simon, A. (2017). Hexanediol: a chemical probe to investigate the material properties of membrane-less compartments. Matters (Zur.).

Liang, M., Xie, X., Pan, J., Jin, G., Yu, C., and Wei, Z. (2019). Structural basis of the target-binding mode of the G protein-coupled receptor kinase-interacting protein in the regulation of focal adhesion dynamics. J. Biol. Chem. *294*, 5827–5839.

Lu, Y., Wu, T., Gutman, O., Lu, H., Zhou, Q., Henis, Y.I., and Luo, K. (2020). Phase separation of TAZ compartmentalizes the transcription machinery to promote gene expression. Nat. Cell Biol. *22*, 453–464.

McDonald, N.A., Fetter, R.D., and Shen, K. (2020). Assembly of synaptic active zones requires phase separation of scaffold molecules. Nature *588*, 454–458.

Ohtsuka, T., Takao-Rikitsu, E., Inoue, E., Inoue, M., Takeuchi, M., Matsubara, K., Deguchi-Tawarada, M., Satoh, K., Morimoto, K., Nakanishi, H., and Takai, Y. (2002). Cast: a novel protein of the cytomatrix at the active zone of synapses that forms a ternary complex with RIM1 and munc13-1. J. Cell Biol. *158*, 577–590.

Olsen, O., Moore, K.A., Fukata, M., Kazuta, T., Trinidad, J.C., Kauer, F.W., Streuli, M., Misawa, H., Burlingame, A.L., Nicoll, R.A., and Bredt, D.S. (2005). Neurotransmitter release regulated by a MALS-liprin-alpha presynaptic complex. J. Cell Biol. *170*, 1127–1134.

Otwinowski, Z., and Minor, W. (1997). Processing of X-ray Diffraction Data Collected in Oscillation Mode. Methods Enzymol. *276*, 307–326.

Patel, M.R., Lehrman, E.K., Poon, V.Y., Crump, J.G., Zhen, M., Bargmann, C.I., and Shen, K. (2006). Hierarchical assembly of presynaptic components in defined C. elegans synapses. Nat. Neurosci. *9*, 1488–1498.

Petzoldt, A.G., Lützkendorf, J., and Sigrist, S.J. (2016). Mechanisms controlling assembly and plasticity of presynaptic active zone scaffolds. Curr. Opin. Neurobiol. *39*, 69–76.

Popp, M.W.-L., and Ploegh, H.L. (2011). Making and breaking peptide bonds: protein engineering using sortase. Angew. Chem. Int. ed. Engl. *50*, 5024–5032.

Sakamoto, H., Ariyoshi, T., Kimpara, N., Sugao, K., Taiko, I., Takikawa, K., Asanuma, D., Namiki, S., and Hirose, K. (2018). Synaptic weight set by Munc13-1 supramolecular assemblies. Nat. Neurosci. *21*, 41–49.

Sala, K., Corbetta, A., Minici, C., Tonoli, D., Murray, D.H., Cammarota, E., Ribolla, L., Ramella, M., Fesce, R., Mazza, D., et al. (2019). The ERC1 scaffold protein implicated in cell motility drives the assembly of a liquid phase. Sci. Rep. *9*, 13530.

Schoch, S., Castillo, P.E., Jo, T., Mukherjee, K., Geppert, M., Wang, Y., Schmitz, F., Malenka, R.C., and Südhof, T.C. (2002). RIM1alpha forms a protein scaffold for regulating neurotransmitter release at the active zone. Nature *415*, 321–326.

Serra-Pagès, C., Medley, Q.G., Tang, M., Hart, A., and Streuli, M. (1998). Liprins, a family of LAR transmembrane protein-tyrosine phosphatase-interacting proteins. J. Biol. Chem. *273*, 15611–15620.

Sigrist, S.J., and Schmitz, D. (2011). Structural and functional plasticity of the cytoplasmic active zone. Curr. Opin. Neurobiol. *21*, 144–150.

Spangler, S.A., Jaarsma, D., De Graaff, E., Wulf, P.S., Akhmanova, A., and Hoogenraad, C.C. (2011). Differential expression of liprin-α family proteins in the brain suggests functional diversification. J. Comp. Neurol. *519*, 3040–3060.

Spangler, S.A., Schmitz, S.K., Kevenaar, J.T., de Graaff, E., de Wit, H., Demmers, J., Toonen, R.F., and Hoogenraad, C.C. (2013). Liprin-α2 promotes the presynaptic recruitment and turnover of RIM1/CASK to facilitate synaptic transmission. J. Cell Biol. *201*, 915–928.

Storoni, L.C., McCoy, A.J., and Read, R.J. (2004). Likelihood-enhanced fast rotation functions. Acta Crystallogr. D Biol. Crystallogr. *60*, 432–438.

Stryker, E., and Johnson, K.G. (2007). LAR, liprin alpha and the regulation of active zone morphogenesis. J. Cell Sci. *120*, 3723–3728.

Südhof, T.C. (2012). The presynaptic active zone. Neuron *75*, 11–25.

Südhof, T.C. (2013). Neurotransmitter release: the last millisecond in the life of a synaptic vesicle. Neuron *80*, 675–690.

Tang, A.-H., Chen, H., Li, T.P., Metzbower, S.R., MacGillavry, H.D., and Blanpied, T.A. (2016). A trans-synaptic nanocolumn aligns neurotransmitter release to receptors. Nature *536*, 210–214.

Taru, H., and Jin, Y. (2011). The Liprin homology domain is essential for the homomeric interaction of SYD-2/Liprin-α protein in presynaptic assembly. J. Neurosci. *31*, 16261–16268.

Terwilliger, T.C., Adams, P.D., Read, R.J., McCoy, A.J., Moriarty, N.W., Grosse-Kunstleve, R.W., Afonine, P.V., Zwart, P.H., and Hung, L.W. (2009). Decision-making in structure solution using Bayesian estimates of map quality: the PHENIX AutoSol wizard. Acta Crystallogr. D Biol. Crystallogr. *65*, 582–601.

Wang, Y., Liu, X., Biederer, T., and Südhof, T.C. (2002). A family of RIM-binding proteins regulated by alternative splicing: Implications for the genesis of synaptic active zones. Proc. Natl. Acad. Sci. USA *99*, 14464–14469.

Wang, S.S.H., Held, R.G., Wong, M.Y., Liu, C., Karakhanyan, A., and Kaeser, P.S. (2016). Fusion Competent Synaptic Vesicles Persist upon Active Zone Disruption and Loss of Vesicle Docking. Neuron *91*, 777–791.

Wei, Z., Zheng, S., Spangler, S.A., Yu, C., Hoogenraad, C.C., and Zhang, M. (2011). Liprin-mediated large signaling complex organization revealed by the liprin-α/CASK and liprin-α/liprin-β complex structures. Mol. Cell *43*, 586–598.

Wentzel, C., Sommer, J.E., Nair, R., Stiefvater, A., Sibarita, J.B., and Scheiffele, P. (2013). mSYD1A, a mammalian synapse-defective-1 protein, regulates synaptogenic signaling and vesicle docking. Neuron *78*, 1012–1023.

Wong, M.Y., Liu, C., Wang, S.S.H., Roquas, A.C.F., Fowler, S.C., and Kaeser, P.S. (2018). Liprin-α3 controls vesicle docking and exocytosis at the active zone of hippocampal synapses. Proc. Natl. Acad. Sci. USA *115*, 2234–2239.

Wu, X., Cai, Q., Shen, Z., Chen, X., Zeng, M., Du, S., and Zhang, M. (2019). RIM and RIM-BP Form Presynaptic Active-Zone-like Condensates via Phase Separation. Mol. Cell *73*, 971–984.e5.

Xie, X., Luo, L., Liang, M., Zhang, W., Zhang, T., Yu, C., and Wei, Z. (2020). Structural basis of liprin-α-promoted LAR-RPTP clustering for modulation of phosphatase activity. Nat. Commun. *11*, 169.

Zeng, M., Shang, Y., Araki, Y., Guo, T., Huganir, R.L., and Zhang, M. (2016). Phase Transition in Postsynaptic Densities Underlies Formation of Synaptic Complexes and Synaptic Plasticity. Cell *166*, 1163–1175.e12.

Zhen, M., and Jin, Y. (1999). The liprin protein SYD-2 regulates the differentiation of presynaptic termini in C. elegans. Nature *401*, 371–375.

Zhu, J., Zhou, Q., Xia, Y., Lin, L., Li, J., Peng, M., Zhang, R., and Zhang, M. (2020). GIT/PIX Condensates Are Modular and Ideal for Distinct Compartmentalized Cell Signaling. Mol. Cell *79*, 782–796.e6.

Zürner, M., and Schoch, S. (2009). The mouse and human Liprin-alpha family of scaffolding proteins: genomic organization, expression profiling and regulation by alternative splicing. Genomics *93*, 243–253.

Zürner, M., Mittelstaedt, T., tom Dieck, S., Becker, A., and Schoch, S. (2011). Analyses of the spatiotemporal expression and subcellular localization of liprin-α proteins. J. Comp. Neurol. *519*, 3019–3039.

STAR★METHODS

KEY RESOURCES TABLE

REAGENT or RESOURCE	SOURCE	IDENTIFIER
Antibodies		
Mouse monoclonal anti-GFP	Transgen	Cat# HT801
Mouse monoclonal anti-liprin-α2	Santa cruz	Cat# sc-393299
Anti-mouse IgG, HRP-linked Antibody	Cell signaling	Cat# 7076S
Bacterial and virus strains		
Escherichia coli BL21 (DE3) cells	AlpaLife by KangTi	Cat# KTSM104L
Chemicals, peptides, and recombinant proteins		
0.25% Trypsin-EDTA	GIBCO	Cat# 25200-072
Lipofectamine 3000 reagent	Invitrogen	Cat# L3000-015
Dulbecco's Modified Eagle Medium (DMEM)	CORNING	Cat# 10-013-CVRC
Fetal bovine serum (FBS)	PAN BIOTECH	Cat# P30-3302
Chemicals: Cy3 NHS ester	AAT Bioquest	Cat# 141
Chemicals: iFluor 405 succinimidyl ester	AAT Bioquest	Cat# 1021
Chemicals: Alexa Fluor 647 NHS Ester	Thermo Fisher	Cat# A2006
Chemicals: 1,6-Hexanediol	Sigma-Aldrich	Cat# H11807
Recombinant protein: liprin-α2_CC1(aa 24-235)	This paper	N/A (custom-made)
Recombinant protein: liprin-α2_CC1-R194C (aa 24-235, R194C)	This paper	N/A (custom-made)
Recombinant protein: liprin-α2_CC1-R194E (aa 24-235, R194E)	This paper	N/A (custom-made)
Recombinant protein: liprin-α2_CC1-L177Q (aa 24-235, L177Q)	This paper	N/A (custom-made)
Recombinant protein: liprin-α2_CC2 (aa 259-542)	This paper	N/A (custom-made)
Recombinant protein: liprin-α2_CC12 (aa 24-542)	This paper	N/A (custom-made)
Recombinant protein: liprin-α2_CC12-R194C (aa 24-542, R194C)	This paper	N/A (custom-made)
Recombinant protein: liprin-α2_H23 (aa 102-235)	This paper	N/A (custom-made)
Recombinant protein: liprin-α2_H23-R194C (aa 102-235, R194C)	This paper	N/A (custom-made)
Recombinant protein: liprin-α2_H2 (aa 102-163)	This paper	N/A (custom-made)
Recombinant protein: liprin-α2_H2-C143A (aa 102-163, C143A)	This paper	N/A (custom-made)
Recombinant protein: liprin-α2_H2-C143A-L141Q (aa 102-163, C143A, L141Q)	This paper	N/A (custom-made)
Recombinant protein: liprin-α2_H2ΔC (aa 102-150)	This paper	N/A (custom-made)
Recombinant protein: liprin-α2_H2-C143A-L141Q (aa 102-163, C143A, L141Q)	This paper	N/A (custom-made)
Recombinant protein: liprin-α2_H2ΔC (aa 102-150)	This paper	N/A (custom-made)

(*Continued on next page*)

Continued

REAGENT or RESOURCE	SOURCE	IDENTIFIER
Recombinant protein: liprin-α2_H2ΔC-L106M-C143A (aa 102-150 L106M, C143A)	This paper	N/A (custom-made)
Recombinant protein: liprin-α2_H3 (aa 164-235)	This paper	N/A (custom-made)
Recombinant protein: liprin-α2_H3-R194C (aa 164-235, R194C)	This paper	N/A (custom-made)
Recombinant protein: liprin-α2_H3-L177Q (aa 164-235, L177Q)	This paper	N/A (custom-made)
Recombinant protein: ELKS1_N (aa 1-581)	This paper	N/A (custom-made)
Recombinant protein: ELKS1_NΔIDR (aa 128-581)	This paper	N/A (custom-made)
Recombinant protein: ELKS2_N (aa 1-577)	This paper	N/A (custom-made)
Recombinant protein: ELKS2_NΔIDR (aa 118-577)	This paper	N/A (custom-made)
Recombinant protein: ELKS2_C (aa 578-957)	This paper	N/A (custom-made)
Recombinant protein: ELKS2_N PBMΔGIWA (aa 1-577+933-953)	This paper	N/A (custom-made)
Recombinant protein: RIM1α_PASB (aa 481-1334)	Wu et al., 2019	N/A
Recombinant protein: RIM1α_C2B (aa 785-1334)	This paper	N/A (custom-made)
Recombinant protein: RIM1α_N-LPETGG (aa 1-474-LPETGG)	Wu et al., 2019	N/A
Recombinant protein: RIM1α_FL (1-1334)	Wu et al., 2019	N/A
Recombinant protein: RBP2-(SH3)$_3$ (aa 178-252+844-1040)	Wu et al., 2019	N/A
Recombinant protein: Sortase A-ΔN59 (aa 60-206)	Popp and Ploegh, 2011	N/A
Recombinant protein: NCav-CT (aa 2151-2327)	Wu et al., 2019	N/A
Recombinant protein: GFP (aa 1-238)	This paper	N/A (custom-made)
Critical commercial assays		
Western ECL substrate	BIO-RAD	Cat# 170-5061
Deposited data		
Crystal structure of Liprinα2 H2ΔC	This paper	PDB code: 7D2G
Crystal structure of Liprinα2 H3	This paper	PDB code: 7D2E
Crystal structure of Liprinα2 H2	This paper	PDB code: 7D2H
Experimental models: Cell lines		
HEK293-T	ATCC	Cat# CRL-11268
Recombinant DNA		
Plasmid: ptCherryC1-liprin-α2 (aa 1-1257)	This paper	N/A (custom-made)
Plasmid: ptCherryC1-liprin-α2 ΔCC1 (aa 236-1257)	This paper	N/A (custom-made)
Plasmid: 32m3c-liprin-α2_CC1 (aa 24-235)	This paper	N/A (custom-made)
Plasmid: 32m3c-liprin-α2_CC1-R194C (aa 24-235, R194C)	This paper	N/A (custom-made)
Plasmid: 32m3c-liprin-α2_CC1-R194E (aa 24-235, R194E)	This paper	N/A (custom-made)
Plasmid: 32m3c-liprin-α2_CC1-L177Q (aa 24-235, L177Q)	This paper	N/A (custom-made)
Plasmid: 32m3c-liprin-α2_CC2 (aa 259-542)	This paper	N/A (custom-made)

(*Continued on next page*)

Continued

REAGENT or RESOURCE	SOURCE	IDENTIFIER
Plasmid: pET28a-liprin-α2_CC12 (aa 24-542)	This paper	N/A (custom-made)
Plasmid: pET28a-liprin-α2_CC12-R194C (aa 24-542, R194C)	This paper	N/A (custom-made)
Plasmid: 32m3c-liprin-α2_H23 (aa 102-235)	This paper	N/A (custom-made)
Plasmid: 32m3c-liprin-α2_H23-R194C (aa 102-235, R194C)	This paper	N/A (custom-made)
Plasmid: 32m3c-liprin-α2_H2 (aa 102-163)	This paper	N/A (custom-made)
Plasmid: 32m3c-liprin-α2_H2-C143A (aa 102-163, C143A)	This paper	N/A (custom-made)
Plasmid: 32m3c-liprin-α2_H2-C143A-L141Q (aa 102-163, C143A, L141Q)	This paper	N/A (custom-made)
Plasmid: 32m3c-liprin-α2_H2ΔC (aa 102-150)	This paper	N/A (custom-made)
Plasmid: 32m3c-liprin-α2_H2ΔC-L106M-C143A (aa 102-150, L106M, C143A)	This paper	N/A (custom-made)
Plasmid: 32m3c-liprin-α2_H3 (aa 164-235)	This paper	N/A (custom-made)
Plasmid: 32m3c-liprin-α2_H3-R194C (aa 164-235, R194C)	This paper	N/A (custom-made)
Plasmid: 32m3c-liprin-α2_H3-L177Q (aa 164-235, L177Q)	This paper	N/A (custom-made)
Plasmid: ptGFP-ELKS1 (aa 1-948)	This paper	N/A (custom-made)
Plasmid: ptGFP-ELKS1_IDR (aa 1-127)	This paper	N/A (custom-made)
Plasmid: ptGFP-ELKS1_ΔIDR (aa 128-948)	This paper	N/A (custom-made)
Plasmid: ptGFP-ELKS1_N (aa 1-581)	This paper	N/A (custom-made)
Plasmid: PETL7-ELKS1_N (aa 1-581)	This paper	N/A (custom-made)
Plasmid: pETL7-ELKS1_ NΔIDR (aa 128-581)	This paper	N/A (custom-made)
Plasmid: ptGFP-ELKS2 (aa 1-957)	This paper	N/A (custom-made)
Plasmid: ptGFP-ELKS2_IDR (aa 1-117)	This paper	N/A (custom-made)
Plasmid: ptGFP-ELKS2_ΔIDR (aa 118-957)	This paper	N/A (custom-made)
Plasmid: ptGFP-ELKS2_N (aa 1-577)	This paper	N/A (custom-made)
Plasmid: pETL7-ELKS2_N (aa 1-577)	This paper	N/A (custom-made)
Plasmid: pETL7-ELKS2_NΔIDR (aa 118-577)	This paper	N/A (custom-made)
Plasmid: pET28a-ELKS2_NΔIDR (aa 118-577)	This paper	N/A (custom-made)
Plasmid: pETL7-ELKS2_C (aa 578-957)	This paper	N/A (custom-made)
Plasmid: pETL7-ELKS2_N PBMΔGIWA(aa 1-577+933-953)	This paper	N/A (custom-made)
Plasmid: m3c-GFP (aa 1-238)	This paper	N/A (custom-made)
Plasmid: pETL7-ELKS2_N (aa 1-577)	This paper	N/A (custom-made)
Plasmid: pETL7-ELKS2_N PBM (aa 1-577+933-957)	This paper	N/A (custom-made)
Plasmid: 32m3c-RIM1α_N-LPETGG (aa 1-474+LPETGG)	Wu et al., 2019	N/A
Plasmid: 32 m-TEV-RIM1α-PASB (aa 481-1334)	Wu et al., 2019	N/A
Plasmid: pET28a-RIM1α_C2B (aa 785-1334)	This paper	N/A (custom-made)
Plasmid: m3c-RBP2-(SH3)$_3$ (aa 178-252+844-1040)	Wu et al., 2019	N/A
Plasmid: Sortase A-ΔN59 (aa 60-206)	Popp and Ploegh, 2011	N/A
Plasmid: 32m3c-NCav-CT (aa 2151-2327)	Wu et al., 2019	N/A

(*Continued on next page*)

Continued

REAGENT or RESOURCE	SOURCE	IDENTIFIER
Software and algorithms		
PHENIX	Adams et al., 2010	https://www.phenix-online.org/
COOT	Emsley and Cowtan, 2004	https://www2.mrc-lmb.cam.ac.uk/personal/pemsley/coot/
PyMOL	Molecular Graphics System, Schrodinger, LLC	https://pymol.org/2/
Origin 7.0	Microcal	https://microcal-origin.software.informer.com/
GraphPad Prism 6	GraphPad Software Inc	https://www.graphpad.com/scientific-software/prism/
ImageJ	NIH	https://imagej.nih.gov/ij/
ASTRA6	Wyatt	https://www.wyatt.com/products/software/astra.html
MO.Affinity Analysis software (V2.3)	NanoTemper Technologies	https://nanotempertech.com/monolith-mo-control-software/
HKL2000 package	Otwinowski and Minor, 1997	https://hkl-xray.com/hkl-2000
PHASER	Storoni et al., 2004	https://www.phaser.cimr.cam.ac.uk/index.php/Phaser_Crystallographic_Software

RESOURCE AVAILABILITY

Lead contact

Further information and requests for resources and reagents should be directed to and will be fulfilled by the lead contact, Zhiyi Wei (weizy@sustech.edu.cn).

Materials availability

Plasmids generated in this study are available from the lead contact by request.

Data and code availability

Coordinates and structure factors of the crystal structures have been deposited in the Protein Data Bank (https://www.wwpdb.org) under the accession code 7D2E (H3), 7D2G (H2ΔC), and 7D2H (H2). All data and are available from the lead contact by request.

EXPERIMENTAL MODEL AND SUBJECT DETAILS

HEK293T cells culture

HEK293T cells (from ATCC) were cultured in DMEM media supported by 10% fetal bovine serum. The HEK293T cells were derived from fetus tissues.

Bacterial strain

Escherichia coli BL21 cells were used in this study for the production of recombinant proteins. Cells were cultured in LB medium supplemented with necessary antibiotics.

METHOD DETAILS

Expression constructs and site-directed mutagenesis

DNA encoding sequences of human liprin-α2 (GenBank: AF034799.1) truncations were subcloned into a modified pET32a vector with an N-terminal thioredoxin (Trx)-His$_6$-tag and an HRV 3C protease cutting site. The CC12 (residues 24 – 542) fragments were cloned into a modified pET28a vector with an N-terminal His$_6$-SUMO tag. H2ΔC (residues 102 – 150) was introduced a L106M/C143A mutation for preparing Se-Met derivative protein. Plasmids containing rat RIM1α (GenBank: XM_017596673.1), RIM-BP2 (GenBank: XM_017598284.1), ELKS1 (GenBank: AY174115.1), ELKS2 (GenBank: AY049038.1), NCav_CT were kind gifts from Dr. Mingjie Zhang. The fragments of rat ELKS1 and ELKS2 used for LLPS assays were subcloned into a modified pETL7 vector with N-terminal His$_6$-MBP-GFP tags and a following TEV-protease cutting site that is kindly provided by Dr. Pilong Li at Tsinghua University. This vector harbors an A206K mutant on the GFP tag to avoid GFP dimerization. The fragments of ELKS1, ELKS2 and RIM1α used for analytical gel filtration were subcloned into a modified pET28a vector with an N-terminal His$_6$-SUMO tag. ELKS2_NPBM was the fusion of ELKS2_N with ELKS2 C-terminal PDZ-binding motif (RSPGRSQHSNHRPSPDQDDEEGIWA). All point mutations were created using site-directed mutagenesis kit and confirmed by DNA sequencing.

Protein preparation

All proteins were expressed in BL21(DE3) *E. coli* cells in LB medium at 16°C. The fusion proteins were purified by Ni^{2+}-NTA affinity chromatography followed by size-exclusion chromatography. The liprin-α2_CC12 protein was further purified by an additional anion exchange column (Mono Q 5/50 GL, GE healthcare) to remove junk proteins after the SUMO-tag cleavage. To prepare the liprin-α2_H2 and H3 fragments for crystallization, the N-terminal His_6-Trx tags were cleaved by HRV 3C protease and removed by a following size-exclusion column (Superdex-200, GE healthcare). The RIM1α full-length protein was generated as previously reported (Popp and Ploegh, 2011; Wu et al., 2019). In brief, the purified RIM1α_N-LPETGG, GGG-RIM1α_PASB, and sortase A-ΔN59 proteins were mixed at ratio of 2:1:1 and the ligation reaction was initiated by adding 10 mM $CaCl_2$ for 2 h at room temperature. The ligated product was further purified through size-exclusion chromatography in a buffer containing 50 mM Tris pH 8.2, 300 mM NaCl, and 2mM DTT.

Protein fluorescence labeling

Cy3/iFluor 405 NHS ester (AAT Bioquest), and Alexa 647 NHS ester (Thermo Fisher) were dissolved by DMSO at stock concentration of 2 mM or 5 mM. Purified proteins were exchanged to the buffer containing 100 mM $NaHCO_3$ pH8.3, 100 mM NaCl, 1 mM EDTA and 2 mM DTT. Fluorophores were mixed with corresponding protein solutions in a 1:1 ratio and incubated at room temperature for 1 hour. The reaction was quenched by adding 200 mM Tris pH 8.2. To remove the unlabeled fluorophores, the labeled proteins were exchanged into a buffer containing 50 mM Tris pH 8.2, 100 mM NaCl, 1mM EDTA and 2mM DTT using a HiTrap desalting column. Fluorescence labeling efficiency was measured by Nanodrop 2000 (ThermoFisher). For imaging assays, fluorescently labeled proteins were added into the corresponding unlabeled proteins in the same buffer with the final molar ratio of 1:100.

Analytical gel filtration chromatography

Analytical gel filtration chromatography was carried out on an ÄKTA pure system (GE Healthcare). Protein samples were loaded into a Superdex 200 Increase 10/300 GL column (GE Healthcare), equilibrated with a buffer containing 50 mM Tris-HCl pH 7.5, 100 mM NaCl, 1 mM EDTA and 2 mM DTT.

Multi-angle light scattering (MALS) analysis

A miniDAWN TREOS (Wyatt Technology Corporation) coupled with an ÄKTA pure system (GE Healthcare) was used for molar mass measurement. The procedure follows the protocol used for analytical gel filtration analysis.

Crystallography

For crystallization, the protein samples were concentrated to ~20 mg/mL. Crystals were obtained by the sitting drop vapor diffusion method at 16°C. To set up a sitting drop, 1 μL of concentrated protein solution was mixed with 1 μL of crystallization solution. The Se-Met derivative crystals of liprin-α2_H2ΔC-L106M&C143A and H3 were grown in the conditions containing 0.2 M Sodium thiocyanate, 20% w/v Polyethylene glycol 3,350 and containing 0.2 M Ammonium acetate, 0.1 M HEPES pH 7.5, 25% w/v Polyethylene glycol 3,350, respectively. The native crystals of liprin-α2_H2-C143A and H3 were grown in the conditions containing 20% v/v 2-Propanol, 0.1 M Tris pH 8.0, 5% w/v Polyethylene glycol 8,000 and containing 0.1 M Sodium citrate tribasic dihydrate pH 5.0, 10% w/v Polyethylene glycol 6,000, respectively. Before X-ray diffraction experiments, crystals were soaked in the crystallization solutions containing additional 30% v/v PEG400 or 35% w/v PEG1000 for cryoprotection. Diffraction data were collected at the Shanghai Synchrotron Radiation Facility beamline BL17U1. Data were processed and scaled using HKL2000 software (Otwinowski and Minor, 1997).

Structure determination and analysis

The crystal structures of liprin-α2_H2ΔC and H3 was determined by using single wavelength anomalous diffraction (SAD) phasing in AutoSol (Terwilliger et al., 2009). The liprin-α2_H2 structure was determined by molecular replacement in PHASER (Storoni et al., 2004) using the H2ΔC structure as the search model. The structural models were refined in PHENIX (Adams et al., 2010) and adjusted in COOT (Emsley and Cowtan, 2004). The model quality was check by MolProbity (Davis et al., 2007). The final refinement statistics are listed in Table 1. The H23 model of liprin-α2 was built by manually replacing a H3 coiled-coil dimer in the H3 tetramer with a H2 coiled-coil dimer. To place the H2 dimer, the sidechains of L141, L144, and V145 were aligned to the sidechains of L177, L174, and V173 in the replaced H3 dimer. All structure figures were prepared by using PyMOL (https://pymol.org/2/).

Isothermal titration calorimetry (ITC) analysis

ITC experiments were carried out on a VP-ITC MicroCal calorimeter (Malvern) at 25°C. All proteins were dissolved in 50 mM Tris buffer containing 100 mM NaCl, 1 mM EDTA, 2 mM DTT at pH 7.5. Each titration point typically is consisted of injecting 10 μL aliquots of one protein in the syringe into its binding protein in the cell. A time interval of 190 s between two titration points was used to ensure the complete equilibrium of each titration reaction.

Microscale thermophoresis (MST) analysis

MST assays were performed on a Monolith NT.115 (NanoTemper Technologies GmbH, Munich, Germany). The Cy3 NHS ester (AAT Bioquest) labeled Trx-H2 (5 μM) was incubated with the serially diluted Trx-H3(WT, R194C or R194E) for 10 min before loading into the capillaries (MO-K022) for Monolith NT.115 analysis. The measurements were performed at 22°C in 50mM HEPES buffer, pH7.5, with 100mM NaCl, 1mM EDTA, by using 40% IR-laser power and 60% LED power. All experiments were independently repeated three times for each measurement. The binding affinity analysis was conducted by MO.Affinity Analysis software (V2.3) and GraphPad Prism 6.

Negative staining and electron microscopy

The liprin-α2_CC12 proteins were eluted as two peaks (oligomers and dimers) during Superdex 200 Increase 10/300 GL column (GE Healthcare), which were analyzed separately by electron microscope. The sample was diluted to 0.05 mg/mL in a buffer containing 50 mM Tris pH 7.5 and 100 mM NaCl and then negative-stained with 2% uranyl acetate. The images were recorded using a transmission electron microscope TEM HT7700 (HITACHI) equipped with a field emission gun and operated at an acceleration voltage of 100 kV.

Co-immunoprecipitation and immunoblotting

For co-immunoprecipitation, transfected HEK293T cells were lysed in ice-cold cell lysis buffer containing 50 mM Tris pH 7.5, 150 mM NaCl, 1% Triton X-100, 5% glycerol, 1 mM phenylmethylsulfonyl fluoride, 1% protease inhibitor cocktail (TargetMol, C001) for 0.5 h at 4°C and followed by centrifugation at 12000 g for 15 min at 4°C. The supernatant fraction was then incubated with anti-GFP conjugated agarose beads (Ktsm-life, ktsm1301) for 1 h at 4°C. The beads were washed with the cell lysis buffer and resuspended with SDS-PAGE sample buffer. The prepared samples were separated by 10% SDS-PAGE and transferred to polyvinylidene difluoride membrane (Millipore, IPVH00010). The membranes were sequentially blocked with 3% BSA in buffer containing 50 mM Tris-HCl pH 7.4, 150 mM NaCl, and 0.1% Tween 20, immunoblotted with antibodies against GFP (TransGen, HT801, dilution 1:3000) or liprin-α2 (Santa cruz, sc-393299, dilution 1:500), probed with horseradish-peroxidase conjugated secondary antibodies (CellSignaling, 7076s, dilution 1:10000) at room temperature and finally developed with a chemiluminescent substrate (BioRad, 107-5061). Protein bands were visualized on the Tanon-6011C Chemiluminescent Imaging System (Tanon Science and Technology).

LLPS assays

All stock proteins were centrifuged at ~20,000 g for 10 minutes at 4°C to remove any precipitations and diluted to designed concentrations with a dilution buffer containing 50 mM Tris pH 7.5, 100 mM NaCl, 1 mM EDTA and 2 mM DTT. To induce LLPS, MBP-GFP tagged ELKS1 and ELKS2 fragments were treated with TEV protease and then dripped onto the wells of the 384-well glass bottom plates (P384-1.5H-N, Cellvis). To produce LLPS of RIM1α/RBP2_(SH3)$_3$, the two proteins were mixed at a 1:1 molar ratio in the dilution buffer. The confocal images were taken by A1R (Nikon) with 100 × oil objective lens. To monitor the proteins in different samples under light microscopes, the unlabeled corresponding proteins were premixed with the fluorophore-labeled proteins of liprin-α2_CC12 (5%), RIM1α (1%), RBP2_(SH3)$_3$ (1%), and NCav_CT (1%).

For sedimentation-based assays, protein samples were diluted with the dilution buffer to total volume of 20 μL. After cleavage at room temperature for 2 hours, the mixture was centrifuged at 1,400 rpm at 22°C for 5 min. The supernatant was immediately isolated by pipette thoroughly and the pellet was re-suspended with 20 μL dilution buffer. Samples from supernatant and pellet were analyzed by 4%–12% gradient SDS-PAGE and Coomassie blue R250 staining. Bands of interest were quantified by ImageJ/Fiji.

For fluorescence imaging, proteins were mixed by pipetting for 3-5 times and dropped onto 384-well plates. Fluorescent images were captured using a Nikon A1R Confocal Microscope at room temperature with a 100 × oil objective lens. The volume of condensates adding on the well was 4-5 μL at the center. For the treatment with 1,6-Hexanediol, assigned concentration of protein and 1,6-Hexanediol were mixed in tubes for 5 min and then dropped onto 384-well plates for imaging. As for the two system-phase imaging, the RIM1α/RBP2_(SH3)$_3$ condensates were injected into the well where the ELKS2_NPBM or ELKS2_NPBM/Liprin α2_CC12-R194C condensates had been settled down for 5 min. During imaging, the 384-well plate was sealed by plastic stickers to reduce solution evaporation. Image fluorescence intensities were analyzed by the ImageJ/Fiji software.

Protein concentration measurements in the condensed phase

The measurement of protein concentration in the LLPS droplets refers to the article reported previously (Wu et al., 2019). The Cy3-labeled liprin-α2_CC12 was premixed with the unlabeled liprin-α2_CC12 or liprin-α2_CC12-R194C to reach the final labeling ratio of 5%. In each measurement, the images were taken in a z stack mode from the bottom of the droplets to 3 μm above with the step interval of 0.15 μm. The highest fluorescent intensity layer was used to calculate individual protein concentration. The Cy3-labeled protein of liprin-α2_CC12 was used to generate the calibration curve of Cy3 intensity by labeled protein concentration. Considering that the ELKS2_N protein fused a GFP at its N terminus, we used the purified His$_6$-GFP protein to generate the calibration curve of GFP intensity by GFP concentration. Fluorescent images were captured using a Nikon A1R Confocal Microscope at room temperature with a 100 × oil objective lens. Images were analyzed with ImageJ/Fiji and the standard curve was fitted by Origin 7.0 software.

Fluorescence recovery after photo-bleaching assay (FRAP)

In vitro FRAP assay was performed on a Nikon A1R confocal microscope with 100 × oil objective lens at room temperature. Fluorescent signals were bleached with corresponding laser beams at 100% power. Pre-bleach and post-bleach images were acquired with no delay time interval. Region of interest (ROI) recovery were monitored for 500 s.

For cellular FRAP experiments, HEK293T cells were plated at low density on 20 mm diameter glass bottom dishes (NEST) coated for 1 hour at 37°C with 10 μg/ml fibronectin (Millipore) and were transfected with the indicated plasmids. Cells were recorded overnight after transfection. Experiments were performed on a Nikon A1R confocal microscope with 60x lens and TOKAI HIT incubator. In full droplet bleaching FRAP experiments, a 2-6 μm diameter circular ROI was bleached, with 100% laser power at 488 nm. After bleaching, images were taken every 5 s for 4.5 minutes to monitor fluorescence recovery. The recovery was measured with ImageJ/Fiji by calculating the fluorescent intensity at each time point and data was corrected with background and normalized with pre-bleaching intensity as 100% and bleaching point intensity as 0%.

Cell culture, transfection and fluorescence imaging

HEK293T cells were cultured in Dulbecco's modification of Eagle's medium (Coring) supplemented with 10% fetal bovine serum (Pan Biotech) and 50 U/ml penicillin and streptomycin. Transfections of indicated plasmids were performed with Lipofectamine 3000 Transfection Reagent (ThermoFisher) according to the manufacturer's instructions. One day after transfection, cells were trypsinized, replated on ~20 μg/ml fibronectin (Millipore)-coated coverslips, and cultured for 3 hours. After fixation with 4% paraformaldehyde, the cells were observed under a Nikon A1R confocal microscope. Images were analyzed using ImageJ/Fiji software.

QUANTIFICATION AND STATISTICAL ANALYSIS

Statistical parameters including the definitions and exact values of n (e.g., number of experiment replications, number of cells, number of droplets, etc) are reported in the figures or corresponding legends. All of the data were expressed as mean ± SD; ns, not significant;*$p < 0.05$,**$p < 0.01$,***$p < 0.001$, and****$p < 0.0001$ using unpaired Student's t test. ITC titration data were analyzed using the program Origin7.0 and fitted by a one-site binding model. MALS data were analyzed in program ASTRA 6.1.2 (Wyatt Technology Corporation) and Origin7.0. Statistical data were conducted in GraphPad Prism 6.

Cell Reports, Volume *34*

Supplemental information

Oligomerized liprin-α promotes phase separation of ELKS for compartmentalization of presynaptic active zone proteins

Mingfu Liang, Gaowei Jin, Xingqiao Xie, Wenchao Zhang, Kaiyue Li, Fengfeng Niu, Cong Yu, and Zhiyi Wei

Supplementary Figures

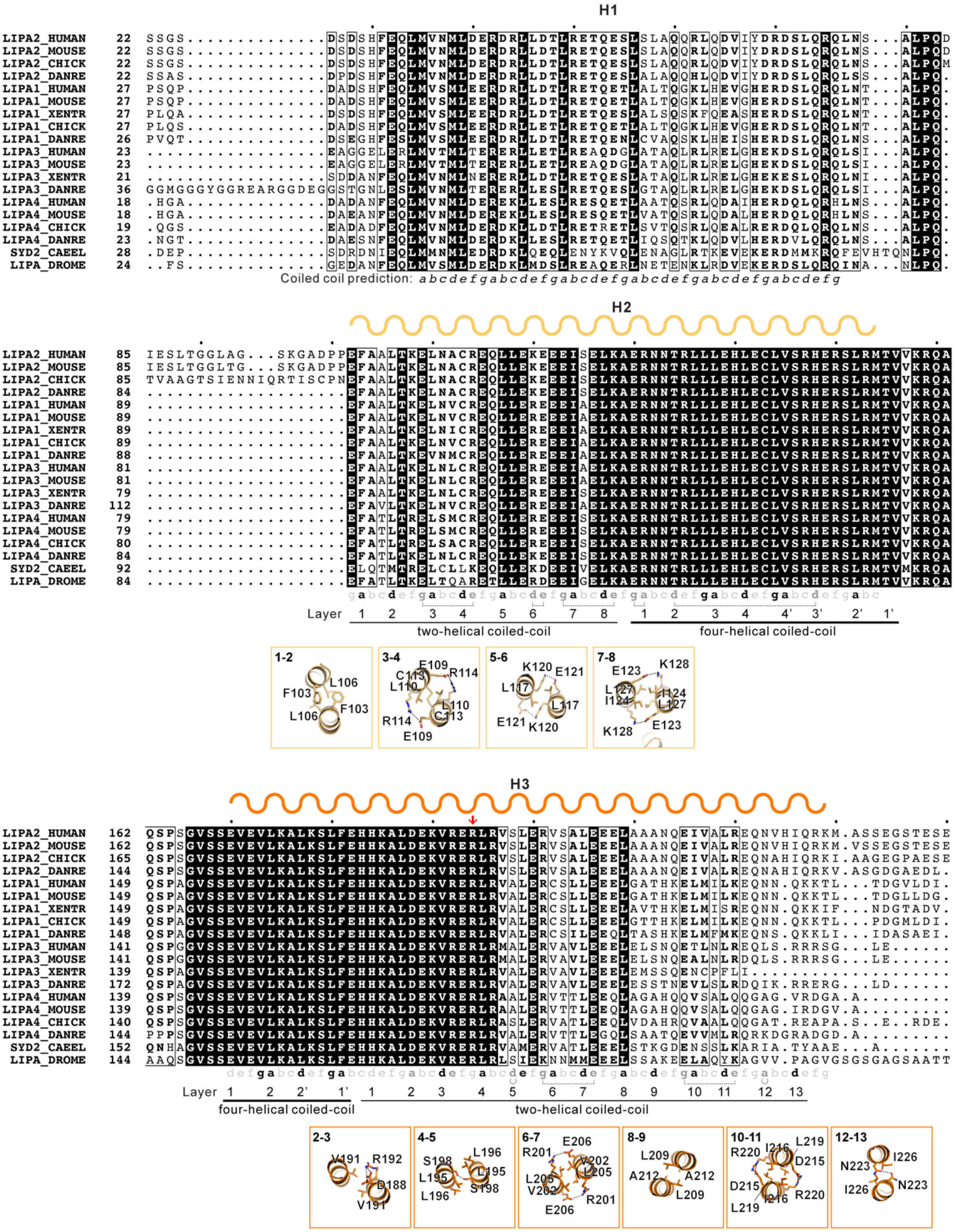

Figure S1. Sequence and structural analysis of the CC1 regions in liprin-α family members.

The amino acid sequence of liprin-αs from human, mouse, chicken, zebrafish, *Drosophila* and *C.elegans* were aligned. Secondary structural elements are indicated above the alignment. R194 in human liprin-α2, corresponding to the gain-of-function mutation site in SYD2 is indicated by a red arrow. Heptad repeats of coiled-coils and layered structural analysis of two-helical coiled-coils in the

CC1 region are indicated below the alignment. Polar interactions are indicated as dashed lines. Related to Figure 1.

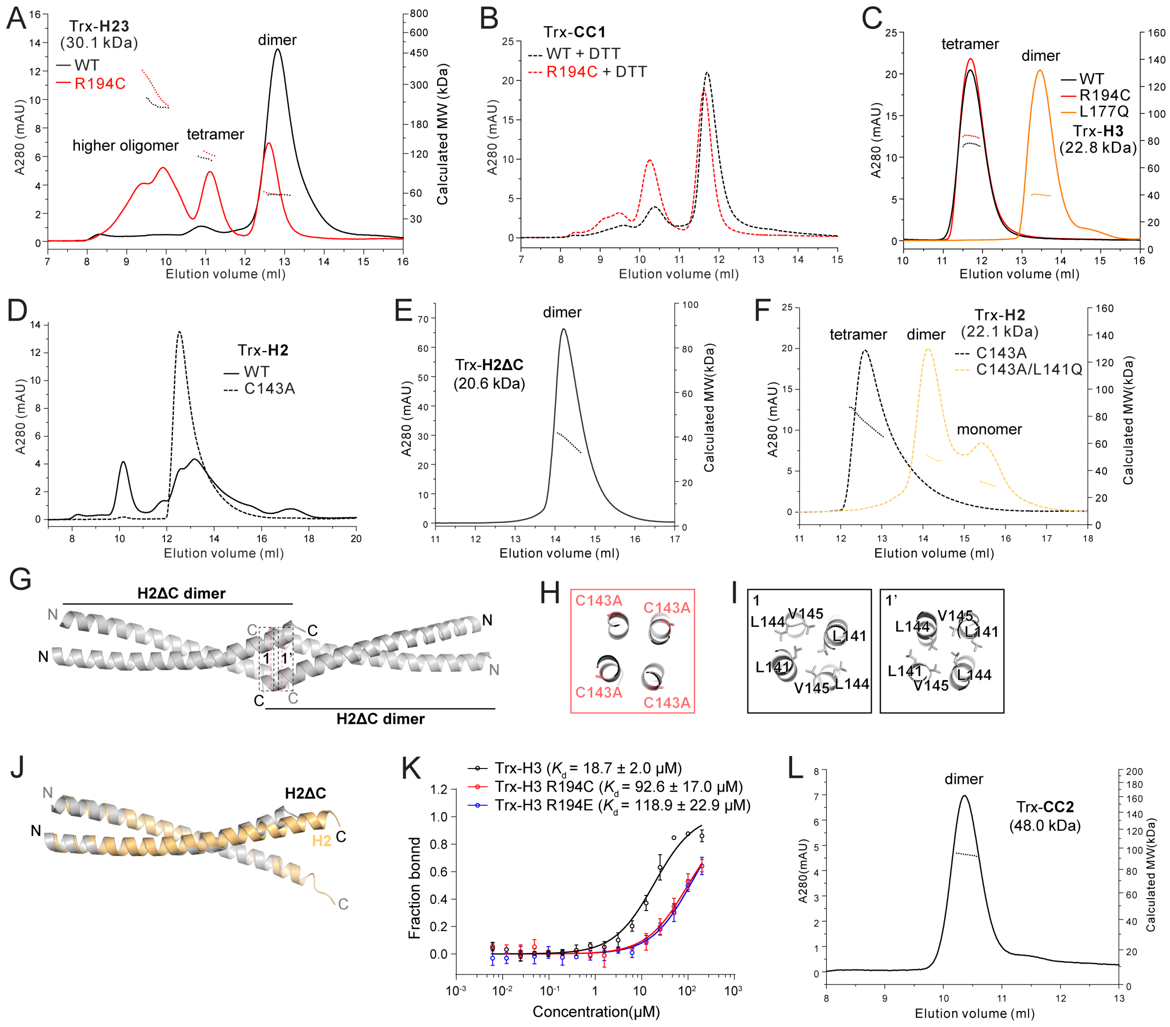

Figure S2. Biochemical and structural analysis of various liprin-α2_CC1 constructs.

(A) Oligomeric analysis of Trx-CC1_H23 and its R194 mutant.

(B) DTT (10 mM) effects on the oligomeric state of Trx-CC1.

(C) Oligomeric analysis of Trx-H3 and its R194C and L177Q mutants.

(D) Analytical gel filtration profiles of Trx-H2 WT and its C143A mutation.

(E) Oligomeric analysis of Trx-H2ΔC.

(F) Oligomeric analysis of the indicated Trx-H2 mutants.

(G) Coiled coil structure of CC1_H2ΔC.

(H) Structural analysis showing the C143 position.

(I) Molecular details of the crystal packing interface between two H2ΔC dimers.

(J) Structural comparison of the H2ΔC and H2 coiled coils.

(K) MST-based analysis of the H2/H3 interaction.

(L) Analytical gel filtration and MASL analysis of the Trx-CC2 dimer.

Related to Figure 1 and 2.

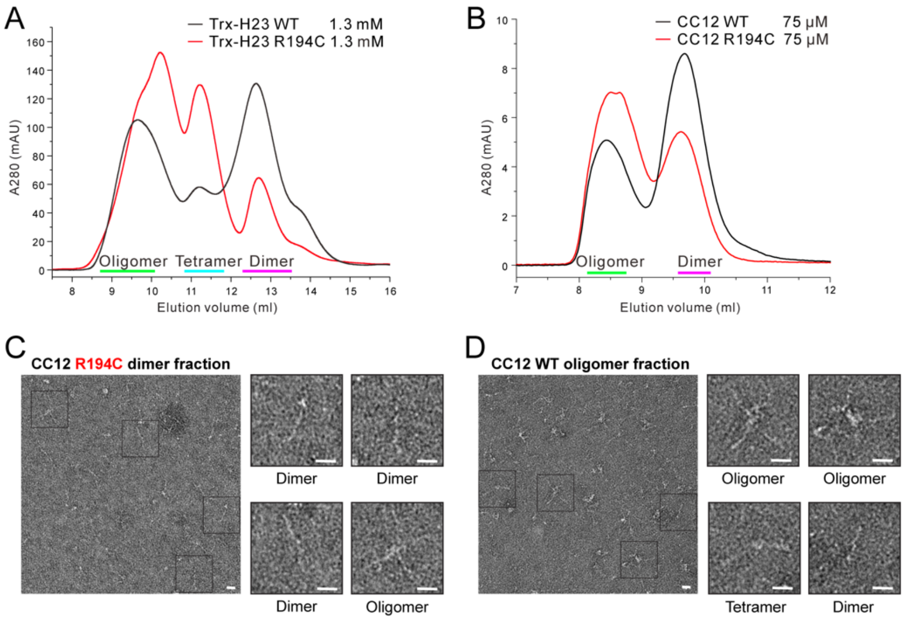

Figure S3. Oligomeric transitions of H23 and CC12.

(A) Oligomeric states of Trx-H23-WT and R194C proteins in a relatively high protein concentration. The oligomer, tetramer and dimer fractions harvested for the rerunning analytical gel filtration (Fig. 3D) are indicated by green, cyan and magenta lines, respectively.

(B) Oligomeric states of CC12-WT and R194C proteins in a relatively high protein concentration. The oligomer and dimer fractions harvested for the rerunning analytical gel filtration (Fig. 3E) are indicated by green and magenta lines, respectively.

(C) Electron microscopic image showing the dimer fraction of CC12-R194C prepared using negative-staining. The particles of CC12-R194C in different oligomeric states were indicated by black boxes and were presented with zoom-in views on the right side. The scale bar is 20nm.

(D) Electron microscopic image showing the oligomer fraction of CC12 prepared using negative-staining. The particles of CC12 in different oligomeric states were indicated by black boxes and were presented with zoom-in views on the right side. The scale bar is 20nm.

Related to Figure 3.

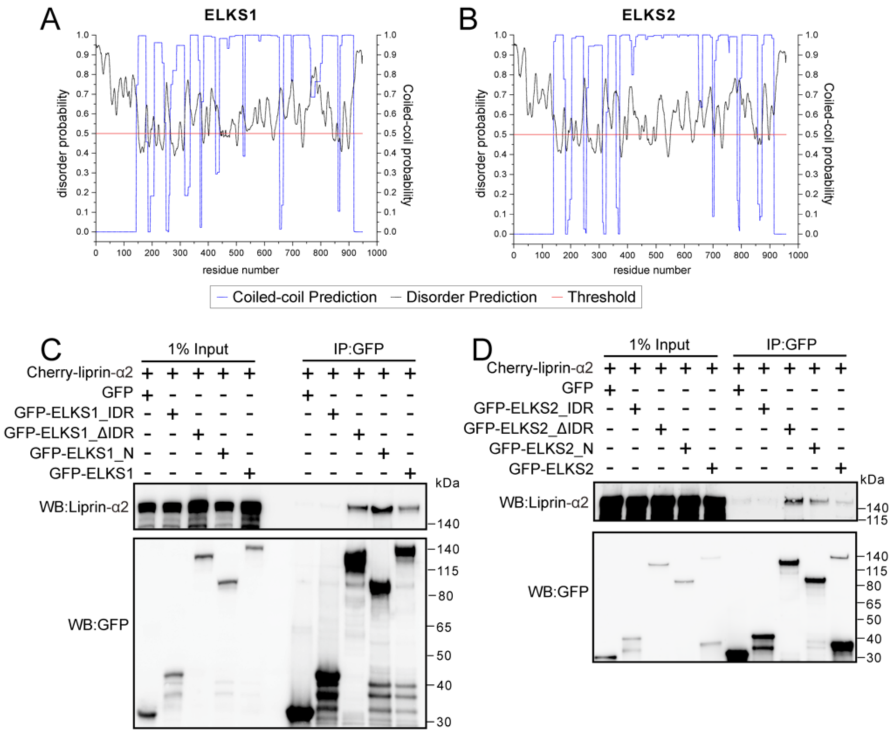

Figure S4. Sequence and interaction analysis of ELKS1/2.

(A&B) Disorder and coiled-coil predictions of ELKS1 (A) and ELKS2 (B). The disorder and coiled-coil predictions were performed by PrDOS (Protein DisOrder prediction system, http://prdos.hgc.jp) and COILS (https://embnet.vital-it.ch/software/COILS_form.html), respectively. The windows width was setting at 28 for the coiled-coil prediction.

(C&D) Co-immunoprecipitation of ELKS1 (C) or ELKS2 (D) with liprin-α2 from lysates of HEK293T cells co-transfected with indicated fragment of GFP-tagged ELKS1 or ELKS2 and Cherry-tagged liprin-α2. The complex was precipitated with anti-GFP agarose beads and immunoblotting with antibodies to liprin-α2 or GFP.

Related to Figure 4.

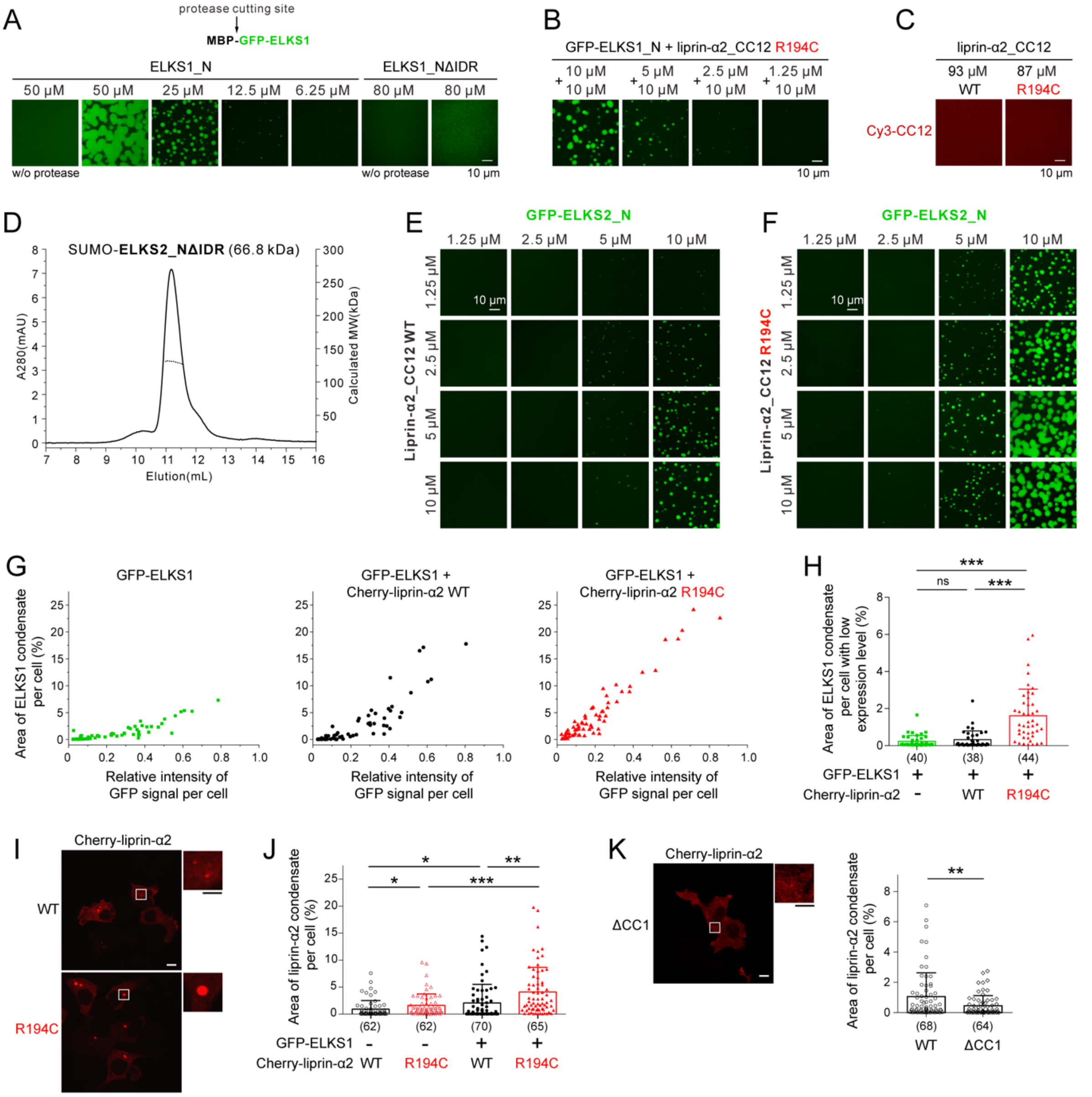

Figure S5. Oligomerized liprin-α2_CC12 promotes the LLPS of ELKS.

(A) Concentration-dependent LLPS of ELKS1. The MBP-tag was cleaved from the fusion proteins to induce LLPS.

(B) Promoted LLPS of ELKS1_N by mixing with liprin-α2 CC12-R194C at different concentrations.

(C) Liprin-α2_CC12 alone failed to form LLPS in solution.

(D) Analytical gel filtration and MALS analysis showing that sumo-ELKS2_NΔIDR is a dimer in solution.

(E&F) Confocal images showing the concentration-dependent promotion of liprin-α2_CC12-WT (E) and R194C (F) on the LLPS of ELKS2_N.

(G) Analysis of condensate area of GFP-ELKS1 per cell plotting against its concentration indicated by GFP signal in HEK-293T cells (Fig. 4L&M). The relative intensity was 1/2000 of measurement intensity.

(H) Quantification of the GFP-ELKS1 clustering levels as shown in (F) with a relative GFP intensity per cell less than 0.2. Data were presented as mean ± SD. ~60 cells per experimental condition. The unpaired Student's t test analysis was used to define a statistically significant difference (*: $p < 0.05$; **: $p < 0.01$; ***: $p < 0.001$; ns: not significant).

(I) Cell imaging of overexpressed Cherry-liprin-α2 with or without the R194C mutation in HEK-293T cells. Scale bar, 10 μm. Regions of interesting were highlighted by boxes and enlarge to 4 times (scale bar, 5 μm).

(J) Quantification of the Cherry-liprin-α2 clustering levels as shown in (I). Data were presented as mean ± SD. ~60 cells per experimental condition.

(K) Cell imaging of overexpressed Cherry-liprin-α2 with the deletion of CC1 in HEK-293T cells. Scale bar, 10 μm. Regions of interesting were highlighted by boxes and enlarge to 4 times (scale bar, 5 μm). Quantification of the clustering levels of Cherry-liprin-α2 with and without the CC1 deletion was shown on the right panel. ~60 cells per experimental condition.

Related to Figure 4.

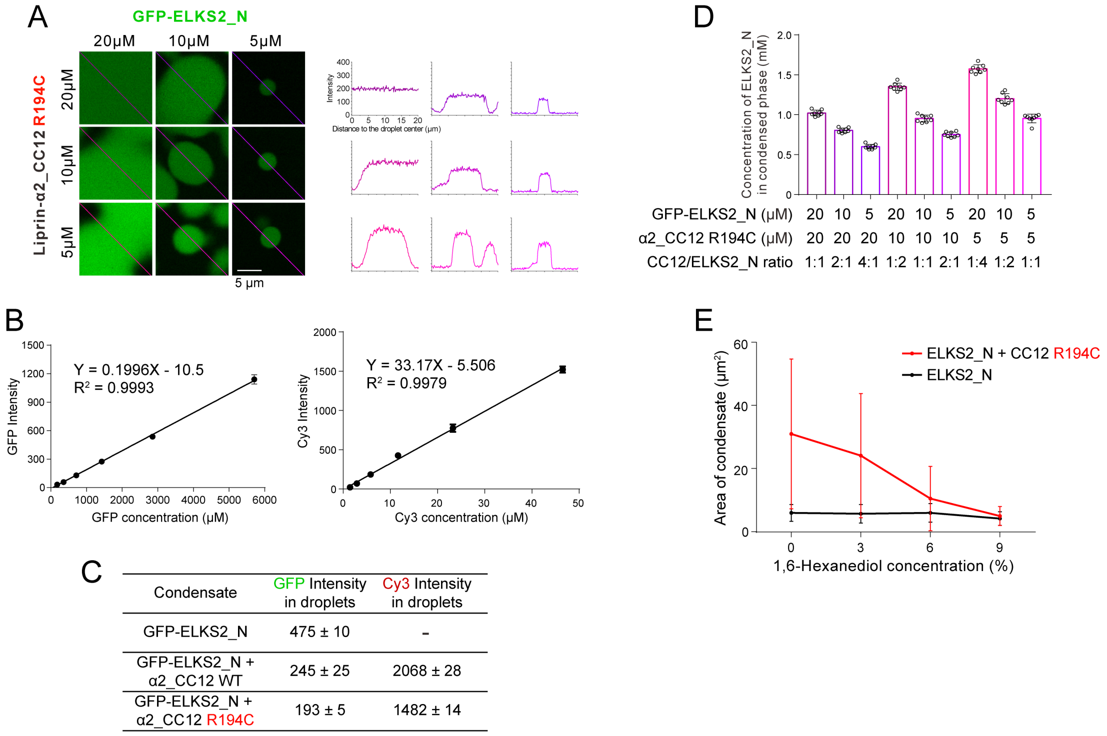

Condensate	GFP Intensity in droplets	Cy3 Intensity in droplets
GFP-ELKS2_N	475 ± 10	-
GFP-ELKS2_N + α2_CC12 WT	245 ± 25	2068 ± 28
GFP-ELKS2_N + α2_CC12 R194C	193 ± 5	1482 ± 14

Figure S6. LLPS analyses of the role of liprin-α2_CC12 in modulating the ELKS2_N condensate.

(A) Confocal microscope-based imaging method to quantify protein concentrations in the condensed droplets. The corresponding intensities are indicated in (D). The results indicate that the initial molar ratio between liprin-α2_CC12 and GFP-ELKS2_N in the mixture determines the dilution fold of GFP-ELKS2_N in the condensed phase.

(B) Standard curves expressing fluorescence intensities of GFP-tagged and Cy3-labeled proteins as a function of concentration. Three repeats were performed for each data point and data were represented as mean ± SD.

(C) Summary table of GFP and Cy3 intensities shown in Fig. 5C.

(D) Calculated concentration of ELKS2_N in the LLPS that shown in (A). The protein concentrations were calculated by using the standard curve shown in (B). Values are presented as mean ± SD from three independent batches of experiments.

(E) Quantification of disrupting effects of different 1,6-Hexanediol concentrations (m/v) on the GFP-ELKS1 condensate with or without CC12-R194C shown in Fig 5I.

Related to Figure 5.

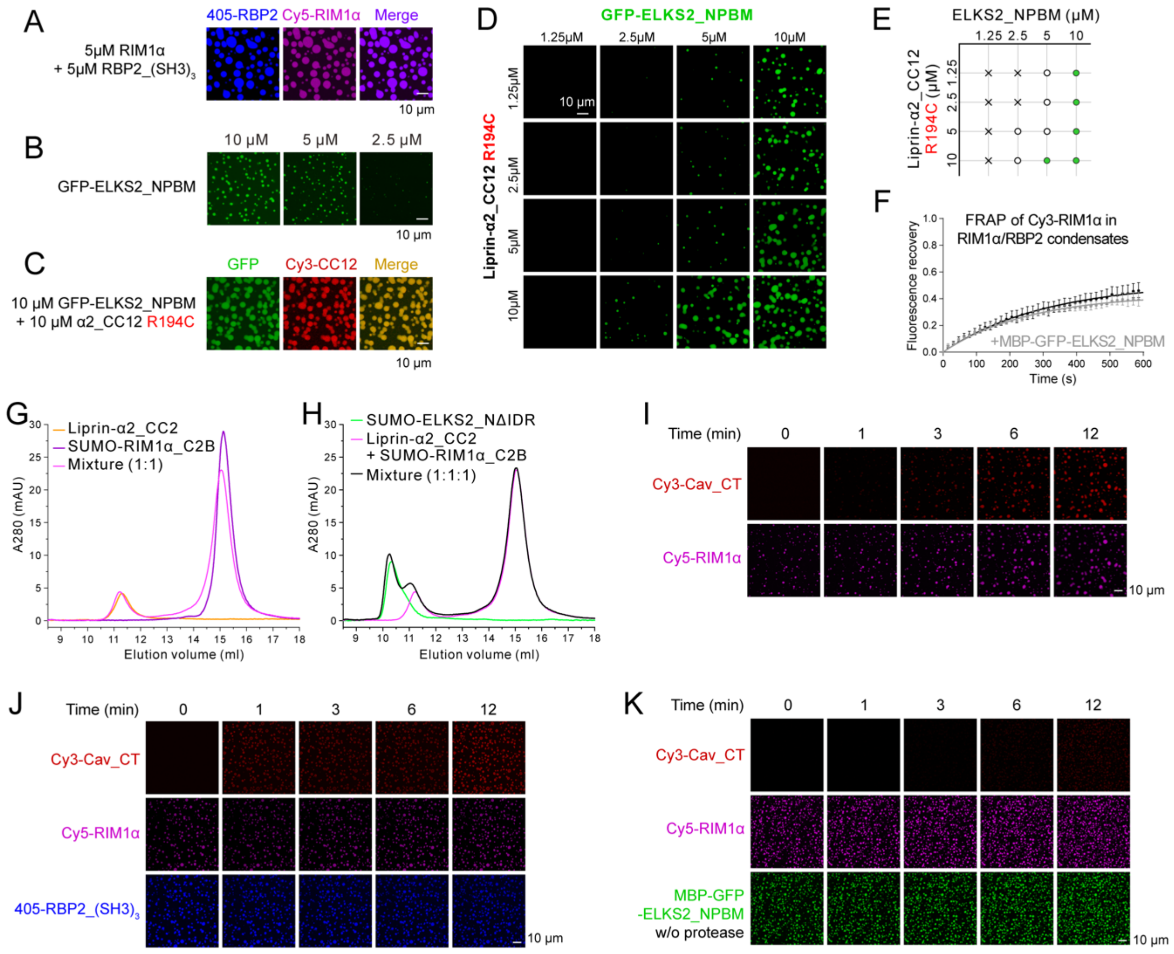

Figure S7. Protein-protein interactions regulate the protein distributions in the ELKS2/liprin-α2 and RIM1α/RBP2 condensates.

(A) The LLPS of RIM1α/RBP2_(SH3)$_3$.

(B) Concentration-dependent LLPS of ELKS2_NPBM.

(C) Enhanced LLPS of ELKS2_NPBM by adding liprin-α2_CC12 R194C.

(D) Confocal images showing the concentration-dependent promotion of liprin-α2_CC12-R194C on the LLPS of ELKS2_NPBM.

(E) Summary plots of the concentration-dependent promotion of liprin-α2_CC12-R194C (D) on the LLPS of ELKS2_NPBM. Open and close circles indicate observation of subtle and obvious phase separations, respectively.

(F) *In vitro* FRAP analysis of the dynamics of the RIM1α molecules in the droplets. The fitting curves represent the averaged signals from 5 droplets and data were presented as mean ± SD.

(G) Analytical gel filtration analysis of the interactions between liprin-α2_CC2 and RIM1α_C2B. The concentration of each protein was 50 μM.

(H) Analytical gel filtration analysis of the complex formation of liprin-α2_CC2, RIM1α_C2B and ELKS2_NΔIDR. The concentration of each protein was 50 μM.

(I) Time-lapse imaging analysis showing the enrichment of NCav_CT in the LLPS of RIM1α. The concentration of each protein was 5 μM.

(J) Time-lapse imaging analysis showing the accelerated enrichment of NCav_CT in the LLPS of RIM1α/RBP2_(SH3)$_3$. The concentration of each protein was 5 μM.

(K) Time-lapse imaging analysis showing little enrichment of NCav_CT in the LLPS of RIM1α preincubated with MBP-GFP-ELKS2_NPBM within the same time scale. The concentration of each protein was 5 μM.

Related to Figure 6.